Control of Ca2+ signals by astrocyte nanoscale morphology at tripartite synapses

Audrey Denizot, Misa Arizono, Valentin Nägerl, Hugues Berry, Erik de Schutter

To cite this version:

Audrey Denizot, Misa Arizono, Valentin Nägerl, Hugues Berry, Erik de Schutter. Control of Ca2+ signals by astrocyte nanoscale morphology at tripartite synapses. Glia, 2022, 10.1002/glia.24258. hal-03582629v1

HAL Id: hal-03582629
https://inria.hal.science/hal-03582629v1

Submitted on 21 Feb 2022 (v1), last revised 12 Oct 2022 (v2)

Control of Ca^{2+} signals by astrocyte nanoscale morphology at tripartite synapses

Audrey Denizot[1*], **Misa Arizono**[2,3], **U. Valentin Nägerl**[2,3], **Hugues Berry**[4,5], **Erik De Schutter**[1]

***For correspondence:**
audrey.denizot3@oist.jp (AD)

[1]Okinawa Institute of Science and Technology, Computational Neuroscience Unit, Onna-Son, Japan; [2]Interdisciplinary Institute for Neuroscience, Université de Bordeaux, Bordeaux, France; [3]Interdisciplinary Institute for Neuroscience, CNRS UMR 5297, Bordeaux, France; [4]Univ Lyon, LIRIS, UMR5205 CNRS, F-69621, Villeurbanne, France; [5]INRIA, F-69603, Villeurbanne, France

---

Abstract Astrocytic Ca^{2+} signals regulate synaptic activity. Most of those signals are spatially restricted to microdomains and occur in fine processes that cannot be resolved by diffraction-limited light microscopy, restricting our understanding of their physiology. Those fine processes are characterized by an elaborate morphology, forming the so-called spongiform domain, which could, similarly to dendritic spines, shapes local Ca^{2+} dynamics. Because of the technical limitations to access the small spatial scale involved, the effect of astrocyte morphology on Ca^{2+} microdomain activity remains poorly understood. Here, we use computational tools and realistic 3D geometries of fine processes based on recent super-resolution microscopy data to investigate the mechanistic link between astrocytic nanoscale morphology and local Ca^{2+} activity. Simulations demonstrate that the nano-morphology of astrocytic processes powerfully shapes the spatio-temporal properties of Ca^{2+} signals and promotes local Ca^{2+} activity. The model predicts that this effect is attenuated upon astrocytic swelling, hallmark of brain diseases, which we confirm experimentally in hypo-osmotic conditions. Upon repeated neurotransmitter release events, the model predicts that swelling hinders astrocytic signal propagation. Overall, this study highlights the influence of the complex morphology of astrocytes at the nanoscale and its remodeling in pathological conditions on neuron-astrocyte communication at tripartite synapses.

Introduction

Astrocytes are glial cells of the central nervous system that are essential for brain development and function, playing key roles in e.g ion homeostasis, neurotransmitters uptake and lactate metabolism (see (***Verkhratsky and Nedergaard, 2018***) for more details). Furthermore, astrocytes can modulate neuronal communication at synapses. In response to the release of neurotransmitters from neurons, Ca^{2+} signals are observed in astrocytes, which can trigger the release of neuroactive molecules by the astrocyte, gliotransmitters. The first type of astrocytic Ca^{2+} signals that has been observed was Ca^{2+} waves that propagate through gap junctions in astrocyte networks (***Giaume and Venance, 1998***). Ca^{2+} waves are also observed within the branches of single astrocytes, sporadically propagating to the soma (***Haustein et al., 2014***; ***Bindocci et al., 2017***). The recent development of Ca^{2+} imaging techniques that provide better spatial and temporal resolution has revealed the existence of spatially-restricted Ca^{2+} signals in astrocytes, referred to as microdomains or hotspots (***Di Castro et al., 2011***; ***Panatier et al., 2011***; ***Stobart et al., 2018a***; ***Srinivasan et al., 2015***; ***Shigetomi et al., 2013***; ***Sherwood et al., 2017***; ***Otsu et al., 2015***; ***Lind et al., 2013***; ***Bindocci et al., 2017***; ***Agarwal et al., 2017***; ***Arizono et al., 2020***). Those local Ca^{2+} signals account for as much as 80 % of astrocytic Ca^{2+} activity and occur in fine astrocytic processes, also referred to as branchlets, which occupy 75 % of the astrocytic volume (***Bindocci et al., 2017***), referred to as the spongiform domain or gliapil. Given that one astrocyte can contact tens of thousands of synapses simultaneously in the mouse hippocampus (***Bushong et al., 2002***) and up to two million in the human brain (***Oberheim et al., 2006***) through these fine processes, local, fast Ca^{2+} signals might enable the astrocyte to powerfully yet precisely control the flow of information through synaptic circuits.

Elaborate cellular morphologies lend themselves to the fine compartmentalization of signals. For example, the anatomical design of dendritic spines restricts the spread of Ca^{2+} to the activated synapse, ensuring that there is little cross-talk between different synapses and that the local Ca^{2+} concentration can go very high (***Santamaria et al., 2011***; ***Tønnesen et al., 2014***; ***Yuste et al., 2000***; ***Noguchi et al., 2005***; ***Yasuda, 2017***; ***Holcman and Schuss, 2011***). It is thus likely that the complex organization of the reticular structure of astrocytes plays a key role in shaping local Ca^{2+} microdomains (***Rusakov, 2015***). For example, the complex shape of Bergmann glia has been proposed to potentially restrict Ca^{2+} signals to the vicinity of synapses (***Grosche et al., 1999***). Similarly, perisynaptic enlargements called “astrocytic compartments” along major branches of astrocytes also exhibit Ca^{2+} signals (***Panatier et al., 2011***). Fine processes of the spongiform domain, however, cannot be resolved by diffraction-limited light microscopy (***Rusakov, 2015***), so that the contribution of their nanoscale morphology to shaping local Ca^{2+} signals is poorly understood. Our recent 3D super-resolution Stimulated Emission Depletion (STED) microscopy study (***Arizono et al., 2020***) revealed that particular shapes of the complex meshwork of astrocytic processes, reminiscent of dendritic spines, are associated with compartmentalized Ca^{2+} signals. Furthermore, aberrant Ca^{2+} signals (***Shigetomi et al., 2019***) and changes in astrocytic morphology, such as “astrocytic swelling”, occur in pathological conditions such as brain injury, including ischemic, traumatic, hemorrhagic and metabolic injuries, stroke and epilepsy (***Lafrenaye and Simard, 2019***). Interestingly, our recent STED study reported that swelling can also occur at the level of fine astrocytic processes (***Arizono et al., 2021a***). The effect of such a remodeling of astrocytic nano-morphology on the local Ca^{2+} signals involved in regulating synapses yet remains unclear. Together, there is a great interest in understanding the mechanistic link between the nano-morphology of astrocytic processes and Ca^{2+} profiles in health and disease. Changing cell morphology experimentally is not straightforward and can affect cell physiology, notably when the osmolarity of the extracellular space is altered. By contrast, computational approaches can finely tune geometrical properties, resulting in more controlled investigations than what could be done experimentally. Computational models are thus tools of choice to investigate the isolated impact of morphological parameters on Ca^{2+} dynamics.

Here, we use computational tools to investigate the effect of astrocyte nanoscale morphology on local Ca^{2+} activity, in healthy and swelling conditions. To account for the stochasticity of molecular interactions in small volumes such as those of astrocyte processes, we use the stochastic voxel-based model of Ca^{2+} signals from Denizot et al. (***Denizot et al., 2019a***). Idealized geometries of branchlets were designed based on super-resolution microscopy images recently reported in live tissue (***Arizono et al., 2020***). Branchlets consist in alternations of structures referred to as nodes and shafts. At this spatial scale, swelling resulting from hypo-osmotic conditions results in an increased diameter of shafts, without altering node morphology (see Fig 3 from (***Arizono et al., 2021b***)). To explore how such changes in morphology affect Ca^{2+} signalling, we performed simulations in geometrical models of branchlets of varying shaft widths. Our simulation results suggest that astrocyte swelling results in an increased diffusion flux, which decreases Ca^{2+} peak probability, duration and amplitude in the stimulated and neighboring nodes. To test those predictions, we performed Ca^{2+} recordings in organotypic hipppocampal cultures in hypo-osmotic conditions, which result in increased shaft width without altering node width. Ca^{2+} activity in hypo-osmotic conditions was decreased compared to Ca^{2+} activity in healthy tissue, in line with our model predictions. In case of repeated node stimulation, thin shafts allowed signal propagation even if some stimuli were omitted. Thin shafts thus allow for more robust signal propagation within the gliapil, which is hindered in swelling conditions.

Overall, this study sheds light on the influence of the nanoscale morphology of the complex spongiform domain of astrocytes on Ca^{2+} microdomain activity. Importantly, our results provide evidence that node compartmentalization, resulting from a reduced diffusion efflux from nodes connected to thin shafts, can increase Ca^{2+} activity locally. Our study indicates that pathological changes in nanoscale astrocyte morphology may substantially affect their Ca^{2+} activity.

Results

Geometrical representation of typical astrocyte processes

In order to investigate the effect of astrocyte nanoscale morphology on the spatio-temporal properties of Ca^{2+} signals, we have designed geometries of typical astrocyte processes, derived from the recent characterization of their ultrastructure at a high spatial resolution (50 nm in x-y) in organotypic hippocampal culture as well as in acute slices and *in vivo* (***Arizono et al., 2020***). Geometries consist of alternations of bulbous structures, nodes, connected to each other with cylindrical structures, referred to as shafts. To reproduce the morphological changes of processes associated with cell swelling reported in hypo-osmotic conditions (Fig 3 in (***Arizono et al., 2021b***)), geometries with different shaft width d_{shaft} and constant node width were designed (Fig 1A). In accordance with node-shaft structures observed experimentally (***Arizono et al., 2020***), node width was set to 380 nm. To model astrocytic Ca^{2+} activity with a high spatial resolution while taking into account the randomness of reactions in small volumes, we used the stochastic voxel-based model from Denizot et al. (***Denizot et al., 2019a***) (see Methods). The reactions included in the model are presented in Fig 1B and in the Methods section. As the majority of Ca^{2+} signals in astrocytes result from the opening of Inositol 3-Phosphate receptors ($\mathrm{IP_3Rs}$), located at the membrane of the endoplasmic reticulum (ER) (***Srinivasan et al., 2015***), signals in the model result from the opening of $\mathrm{IP_3Rs}$ (see Denizot et al. (***Denizot et al., 2019a***) for discussion on the model's assumptions and limitations).

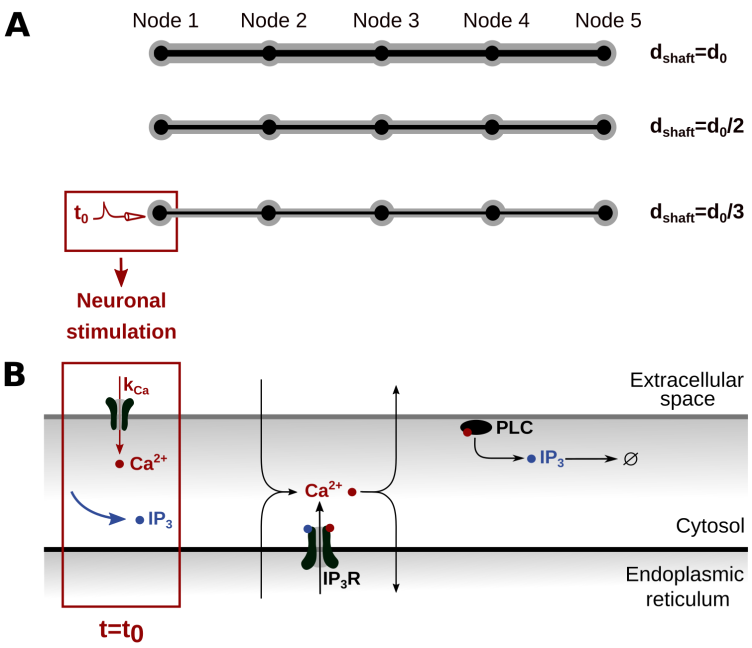

Figure 1. Geometries and kinetic scheme used for simulating Ca^{2+} dynamics in node/shaft structures of the gliapil. (*A*) Geometries reproducing node/shaft geometries of the gliapil (***Arizono et al., 2020***; ***Panatier et al., 2014***) were designed. Nodes are approximated as spheres of diameter 380 nm and shafts as 1 μm-long cylinders. The geometries designed in this study, referred to as "5 nodes", contain 5 identical nodes and 4 identical shafts. Geometries were characterized by different shaft widths: $d_{\mathrm{shaft}} = d_0 = 380nm$, $d_{\mathrm{shaft}} = \frac{d_0}{2}$ and $d_{\mathrm{shaft}} = \frac{d_0}{3}$. The associated cytosolic volume, plasma and ER membrane areas are presented in Table 1. (*B*) Biochemical processes included in the model. Ca^{2+} can enter/exit the cytosol from/to the extracellular space or the endoplasmic reticulum (ER), resulting from the activity of Ca^{2+} channels/pumps. Ca^{2+} and IP_3 diffuse in the cytosol following Brownian motion. The kinetics of IP_3R channels corresponds to the 8-state Markov model from (***Denizot et al., 2019b***), adapted from (***De Young and Keizer, 1992***; ***Bezprozvanny et al., 1991***). When both IP_3 and Ca^{2+} are bound to IP_3R activating binding sites, the IP_3R is in open state and Ca^{2+} enters the cytosol. Ca^{2+} can activate Phospholipase C δ (PLCδ), which results in the production of IP_3. For more details, please refer to (***Denizot et al., 2019b***). Neuronal stimulation is simulated as an infusion of IP_3 in the cytosol and the opening of Ca^{2+} channels at the plasma membrane with an influx rate k_{Ca} (see Methods).

Figure 1–Figure supplement 1. Sensitivity study of the effect of voxel size on Ca^{2+} signals.

Figure 1–source data 1. Characteristics of meshes used to investigate the effect of voxel size on Ca^{2+} signals (Table Supplement 1).

Thin shafts favor node compartmentalization

In order to test whether the geometries designed in this study are a good approximation of the ultrastructure of the gliapil, we have compared molecular diffusion flux in those geometries with those reported experimentally. To do so, we simulated photobleaching experiments and compared our results to experimental results from Arizono et al. (***Arizono et al., 2020***). The principle of bleaching simulations is presented in the Methods section and in Supplemental Movie 1. Here, we refer to an increased node compartmentalization when the time to recovery after bleaching, τ, increases (see Fig 2B).

Bleaching traces in simulations are both qualitatively (Fig 2B) and quantitatively (Fig 2C) similar to experimental bleaching traces, for shaft width $d_{\mathrm{shaft}} = d_0$ and $d_{\mathrm{shaft}} = \frac{d_0}{2}$. Indeed, no significant difference of I_0 (Fig 2C1), I_{inf} (Fig 2C2) and τ (Fig 2C3) was observed between simulations and experimental traces. Simulations were also performed with $d_{\mathrm{shaft}} = \frac{d_0}{3}$. Our simulations successfully reproduce experimental bleaching experiments and suggest that τ, and thus node compartmental-

Table 1. Characteristics of the geometries of astrocyte branchlets used in this study. V_{cyt} is the cytosolic volume, S_{PM} is the area of the plasma membrane and S_{ER} is the area of the ER membrane. Volumes are expressed in nm^3 and areas in nm^2. Meshes are available at http://modeldb.yale.edu/266928, access code: lto42@tpk3D?

Geom	V_{cyt} (nm^3)	S_{PM} (nm^2)	S_{ER} (nm^2)
"5nodes" $d_{\mathrm{shaft}} = d_0$	6.20×10^8	7.73×10^6	2.19×10^6
"5nodes" $d_{\mathrm{shaft}} = d_0/2$	2.63×10^8	4.95×10^6	1.28×10^6
"5nodes" $d_{\mathrm{shaft}} = d_0/3$	1.95×10^8	4.10×10^6	9.99×10^5
"No ER" $d_{\mathrm{shaft}} = d_0$	6.73×10^8	7.73×10^6	0.00
"No ER" $d_{\mathrm{shaft}} = d_0/2$	2.83×10^8	4.95×10^6	0.00
"No ER" $d_{\mathrm{shaft}} = d_0/3$	2.10×10^8	4.09×10^6	0.00
"Node ER" $d_{\mathrm{shaft}} = d_0$	6.67×10^8	7.75×10^6	4.17×10^5
"Node ER" $d_{\mathrm{shaft}} = d_0/2$	2.74×10^8	4.96×10^6	4.37×10^5
"Node ER" $d_{\mathrm{shaft}} = d_0/3$	2.00×10^8	4.11×10^6	4.41×10^5
"Cyl ER" $d_{\mathrm{shaft}} = d_0$	6.27×10^8	7.74×10^6	2.03×10^6
"Cyl ER" $d_{\mathrm{shaft}} = d_0/2$	2.77×10^8	4.95×10^6	8.78×10^5
"Cyl ER" $d_{\mathrm{shaft}} = d_0/3$	2.07×10^8	4.09×10^6	5.86×10^5

ization, increases when shaft width decreases (Fig 2C3). This result is not surprising as a decreased shaft width results in a smaller size of the exit point for diffusing molecules from the node. This is similar to e.g dendritic spines, which compartmentalization is increased for thinner spine necks (***Santamaria et al., 2011***; ***Tønnesen et al., 2014***). The geometries that we have designed can thus be considered as a reasonable approximation of the ultrastructure of the gliapil observed experimentally in live tissue.

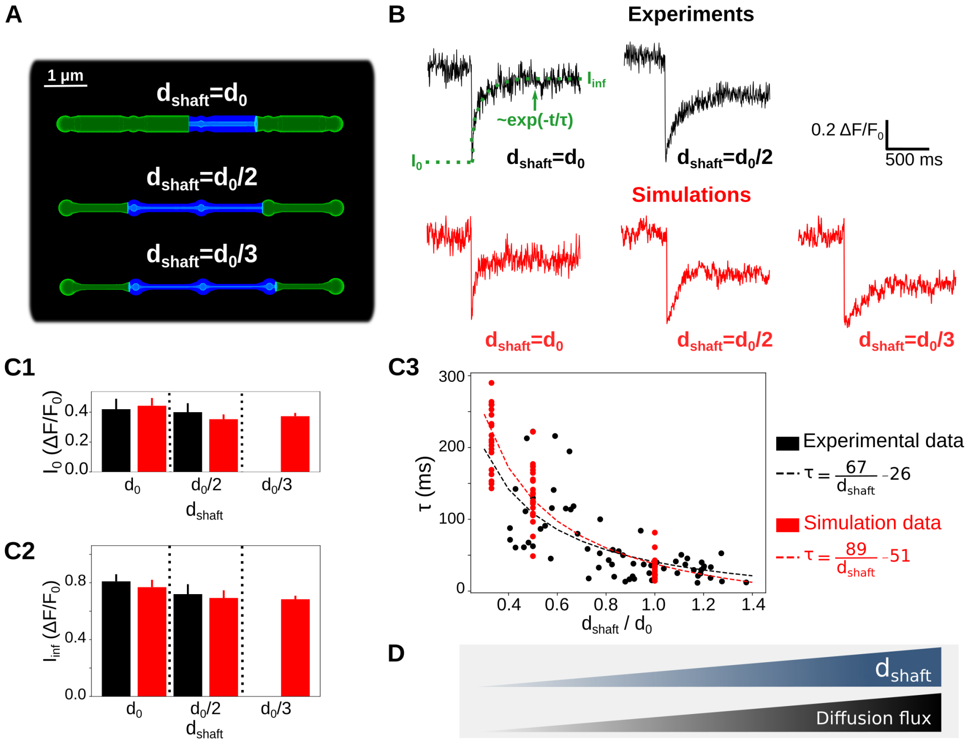

Figure 2. Simulations confirm that thin shafts favor node compartmentalization. (*A*) Geometries of different shaft widths d_{shaft}, $d_{\text{shaft}} = d_0$, $\frac{d_0}{2}$ and $\frac{d_0}{3}$, used in the bleaching simulations. Blue color represents the bleached volume, which varied depending on the value of d_{shaft} in order to fit experimental values of I_0 and I_{inf}. (*B*) Representative experimental (top) and simulation (bottom) traces for different shaft width values. I_0, I_{inf} and τ were calculated using Eq 1. Note that simulations were also performed for $d_{\text{shaft}} = \frac{d_0}{3}$. (*C*) Quantification of I_0 (C1), I_{inf} (C2) and τ (C3) values in simulations (red) compared to experiments (black). Note that no experimental data was available for $d_{\text{shaft}} = \frac{d_0}{3}$. In C1 and C2, n=5×2 and 20×3 for experiments and simulations, respectively. Data are presented as mean ± STD. In C3, n=66 and n=20×3 for experiments and simulations, respectively. τ is negatively correlated to d_{shaft} in experiments (n=66 from 7 slices; Spearman r=-0.72, p<0.001 ***) and simulations (n=60; Spearman r=-0.89, p<0.001 ***). Black and red lines represent curve fit of τ as a function of d_{shaft} of the form $\tau = a * \frac{1}{d_{\text{shaft}}} + b$ for experiments and simulations, respectively. (*D*) Schematic summarizing the conclusion of this figure: diffusion flux increases with d_{shaft}. In that sense, thin shafts favor node compartmentalization. Data in panels C1 and C2 are represented as mean ± STD, n=20 for each geometry.

Figure 2–video 1. Movie of a simulated bleaching experiment, with $d_{\text{shaft}}=\frac{d_0}{2}$. Fluorescing ZsGreen molecules are in red and bleached, non-fluorescing, ZsGreen are in yellow.

Thin shafts enhance Ca^{2+} activity in nodes

80% of astrocyte Ca^{2+} activity occurs in the gliapil (***Bindocci et al., 2017***), which suggests that most neuron-astrocyte communication occurs at fine astrocytic processes. As we observed that a decreased shaft width is associated with a decreased diffusion flux, i.e an increased compartmentalization of nodes, we have tested whether this effect influences Ca^{2+} activity upon neuronal stimulation. To do so, we have first analyzed Ca^{2+} signals resulting from a single neuronal stimulation, which was simulated as an infusion of IP$_3$ and Ca^{2+} in the stimulated node, node 1 (see Methods). Those parameters encompass the IP$_3$ production by phospholipase C following the activation of G_q-G-protein-coupled receptors (GPCRs) resulting from the binding of neuronal glutamate, ATP and noradrenaline to G_q proteins and Ca^{2+} entry at the plasma membrane through Ca^{2+} channels, ionotropic receptors or the sodium/calcium exchanger (NCX) functioning in reverse mode (***Ahmadpour et al., 2021***; ***Semyanov et al., 2020***). Signals were recorded both in the stimulated node, node 1, and in the neighboring node, node 2 (Supplemental Movie 1). Representative Ca^{2+} traces in node 2 for $d_{\text{shaft}} = d_0$, $\frac{d_0}{2}$ and $\frac{d_0}{3}$ are displayed in Fig 3A. Our first result is that Ca^{2+} peak probability increases when d_{shaft} decreases (Fig 3B1). The time to 1^{st} peak increases with d_{shaft} (Fig 3B2). By contrast, peak amplitude (Fig 3B3) and duration (Fig 3B4) increase when d_{shaft} decreases. In order to better understand the mechanisms responsible for the increased Ca^{2+} peak probability, amplitude and duration when d_{shaft} decreases, we have measured the frequency of IP_3R opening in nodes 1 and 2. The frequency of IP_3R opening increases when d_{shaft} decreases (Fig 3B5). Note that the duration of IP_3R opening and the number of IP_3Rs open per Ca^{2+} peak did not vary with d_{shaft}. The increased IP_3R opening frequency associated with small values of d_{shaft} probably results from the increased residency time of molecules in nodes connected to thin shafts (Fig 3C). Indeed, a thin shaft can "trap" Ca^{2+} and IP_3 longer in the node, thus locally increasing the probability of IP_3Rs to open, resulting in larger Ca^{2+} peaks. For more details, the reader can refer to the theoretical work investigating the narrow escape problem for diffusion in microdomains (***Schuss et al., 2007***). Nodes connected to thinner shafts, despite being characterized by a lower diffusion flux (Fig 2), could thus consist of signal amplification units, favoring the generation of larger signals, therefore increasing Ca^{2+} peak probability, amplitude and duration both in the stimulated node and in neighboring nodes.

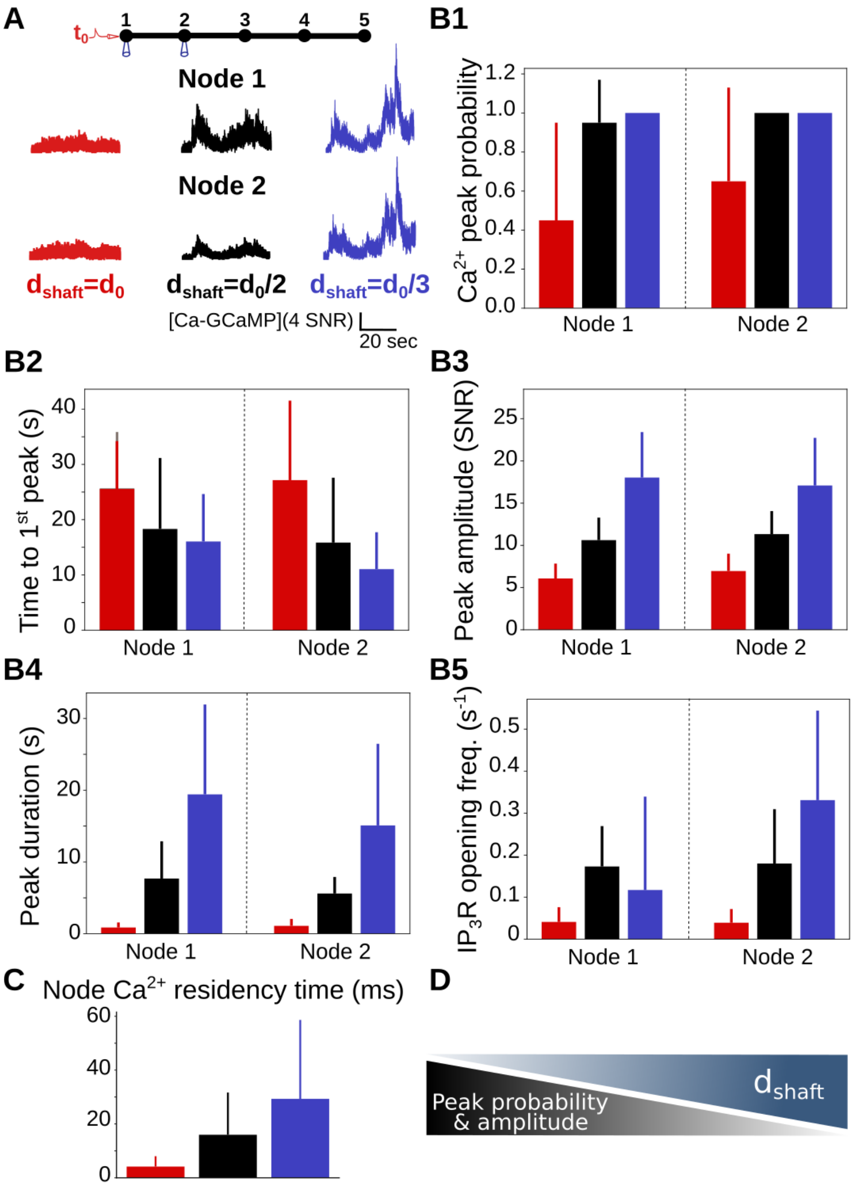

Figure 3. Ca^{2+} **peak probability, amplitude and duration increase when shaft width decreases.** (*A*) (*Top*) Neuronal stimulation protocol simulated for each geometry: node 1 was stimulated at t=t_0=1s, while Ca^{2+} activity was monitored in node 2. Representative Ca^{2+} traces for shaft width $d_{\text{shaft}} = d_0$ (red), $\frac{d_0}{2}$ (black) and $\frac{d_0}{3}$ (blue), expressed as SNR (see Methods). (*B*) Quantification of the effect of d_{shaft} on Ca^{2+} signal characteristics Data are represented as mean ± STD, n=20. Ca^{2+} peak probability increases (***, *B1*), Time to 1^{st} peak decreases (***, *B2*), peak amplitude (***, *B3*) and duration (***, *B4*) increase when d_{shaft} decreases. (*C*) Ca^{2+} residency time in node 1 increases when d_{shaft} decreases (***, n=300). (*D*) Schematic summarizing the main result from this figure: Ca^{2+} peak probability and amplitude increase when shaft width decreases. The effect of d_{shaft} on each Ca^{2+} signal characteristic was tested using one-way ANOVA. Significance is assigned by * for $p \leq 0.05$, ** for $p \leq 0.01$, *** for $p \leq 0.001$.

Figure 3–video 1. Movie of a simulation of the neuronal stimulation protocol, with d_{shaft}=$\frac{d_0}{2}$, k_{Ca}=0 s^{-1}.

Figure 3–Figure supplement 1. Sensitivity study of the effect of d_{shaft} on local Ca^{2+} signals.

Figure 3–Figure supplement 2. Effect of Ca^{2+} influx rate at the plasma membrane on local Ca^{2+} signals.

Figure 3–Figure supplement 3. Sensitivity study of the effect of boundary conditions on local Ca^{2+} activity upon single node stimulation.

Figure 3–Figure supplement 4. Node/shaft width ratio and node volume control local Ca^{2+} activity.

Figure 3–Figure supplement 5. Thin shafts enhance local spontaneous Ca^{2+} activity.

Figure 3–Figure supplement 6. Ca^{2+} peak probability, amplitude and duration decrease with ER surface area.

Figure 3–Figure supplement 7. Local Ca^{2+} activity increases when shaft diameter decreases, for all ER geometries tested.

Figure 3–Figure supplement 8. Sensitivity study of the effect of ER morphology on Ca^{2+} dynamics.

Figure 3–Figure supplement 9. Ca^{2+} indicators alter Ca^{2+} peak characteristics.

To identify the cause of the increased Ca^{2+} activity when shaft width decreases (Fig 3), we performed simulations in which we altered the stimulated node (Supplemental Fig 1D-E), Ca^{2+} influx at the plasma membrane (Supplemental Fig 2) and boundary conditions (Supplemental Fig 3). Those parameters did not affect the observed effects of d_{shaft} on Ca^{2+} dynamics. Furthermore, we repeated simulations of Fig 3 with constant cytosolic volume (Supplemental Fig 4) and constant number of IP_3Rs (Supplemental Fig 1A-C), irrespective of the value of d_{shaft}. Our results confirm that the relevant parameter responsible for the observed effects of d_{shaft} on Ca^{2+} signal characteristics is the node/shaft width ratio or the cytosolic volume rather than d_{shaft} itself. Spontaneous Ca^{2+} signals were affected by shaft width in the same way as neuronal-induced Ca^{2+} signals (Supplemental Fig 5) and, in particular, reproduced the increase of the amplitude ratio of spontaneous Ca^{2+} signals between node 2 and node 1 with shaft width observed in hippocampal organotypic cultures (***Arizono et al., 2020***). Note that ER morphology, in particular ER surface area (Supplemental Fig 6, 7 and 8), and Ca^{2+} buffering by Ca^{2+} indicators (Supplemental Fig 9), consistent with previous reports (***Denizot et al., 2019a***; ***Bartol et al., 2015***; ***Majewska et al., 2000***), can also alter local Ca^{2+} dynamics.

Overall, our results suggest that a decreased shaft width, resulting in a decreased diffusion efflux from nodes, increases Ca^{2+} peak probability, amplitude and duration. Conversely, the swelling of fine processes, resulting in an increase of shaft width, attenuates local Ca^{2+} peak probability, amplitude and duration.

Ca^{2+} imaging confirms that swelling attenuates local spontaneous Ca^{2+} activity

Our recent super-resolution study revealed that the nano-architecture of fine processes is remodeled in hypo-osmotic conditions (***Arizono et al., 2021b***). At this spatial scale, hypo-osmotic conditions resulted in heterogeneous swelling of processes, where shaft width increased while node width remained unaltered (see Fig 3 in (***Arizono et al., 2021b***)). Simulation results presented in Fig 3 suggest that processes with increased shaft width d_{shaft} are associated with decreased Ca^{2+} peak probability, duration and amplitude. To test whether this effect can be observed in live tissue, we thus performed experimental measurements of calcium dynamics in fine astrocytic processes under basal and hypo-osmotic conditions. To resolve Ca^{2+} signals in fine branchlets, we performed experiments using confocal microscopy in organotypic cultures, which provides the best optical access and sample stability in live tissue to date (resolution ≈ 200 nm in x-y versus ≈ 500 nm for two-photon microscopy). In accordance with our model's predictions, Ca^{2+} peak amplitude and duration were lower in hypo-osmotic compared to basal conditions (Fig 4A-D). Note that peak amplitude and duration did not significantly vary when measured repeatedly in basal conditions (Fig 4E-F). Overall, our experimental results confirm that the complex nano-architecture of fine astrocytic processes and its alteration, such as cell swelling, shapes local Ca^{2+} activity.

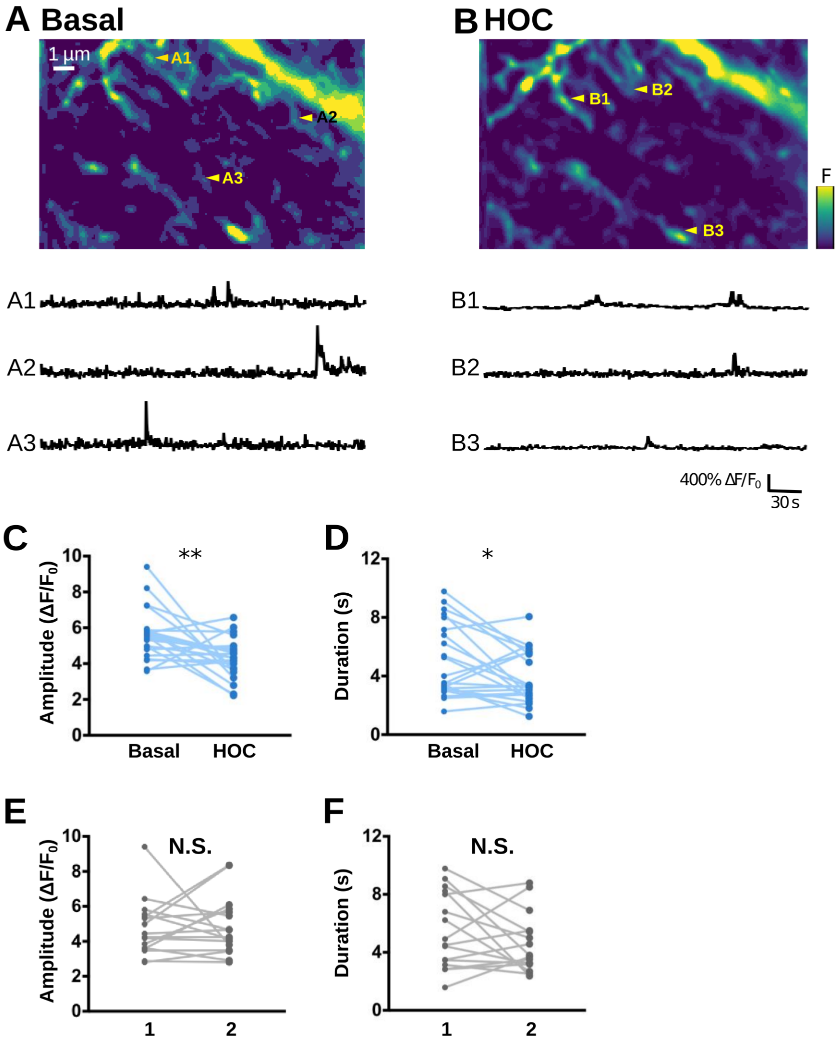

Figure 4. Ca^{2+} **imaging confirms that swelling attenuates local spontaneous** Ca^{2+} **activity.** (*A, B*) (Top) Confocal images of the astrocytic spongiform domain expressing GCaMP6s at baseline (basal, A) and in hypo-osmotic condition (HOC, B), measured in organotypic hippocampal cultures. (Bottom) Representative traces of spontaneous Ca^{2+} events from ROIs indicated in A (A1-A3) and B (B1-B3). (*C, D*) Ca^{2+} peak amplitude (C) and duration (D) of spontaneous Ca^{2+} events are significantly smaller in hypo-osmotic conditions (HOC) compared to basal conditions (Basal). (*E, F*) Amplitude (E) and duration (F) of spontaneous Ca^{2+} events do not significantly vary when measured twice in a row (1, 2) in the absence of HOC. Significance is assigned by * for $p \leq 0.05$, ** for $p \leq 0.01$, *** for $p \leq 0.001$.

Thin shafts favor more robust signal propagation

A single astrocyte branchlet can contact and modulate the activity of multiple synapses, referred to as synaptic clusters, which can belong to the same or to different dendrites or even to different neurons (***Arizono et al., 2020***; ***Reichenbach et al., 2010***; ***Witcher et al., 2007***; ***Cali et al., 2019***; ***Semyanov et al., 2020***). The frequency of stimulation of the branchlet can vary depending on the activity of the adjacent synapses. For example, a connection of adjacent astrocytic nodes to co-active synapses would result in a high node stimulation frequency. We have thus tested the influence of the frequency of neuronal stimulation of neighboring nodes on the propagation of Ca^{2+} signals in branchlets. To do so, we have performed simulations in which neighboring nodes were repeatedly stimulated after a time period τ_{IP3}, that varied from 50 ms to 5s, while Ca^{2+} signals were recorded in a remote node, node 5 (Fig 5A). Neuronal stimulation is simulated as an infusion of 50 IP_3 molecules in the stimulated node. Representative Ca^{2+} traces in node 5 in branchlets with various shaft widths d_{shaft} are presented in Fig 5A for τ_{IP3}=250 and 3000 ms. Our first notable result is that the time to 1^{st} peak in node 5 decreases with d_{shaft} , whatever the value of τ_{IP3} (Fig 5B1). More specifically, time to 1^{st} peak is higher for d_{shaft} =d_0 compared to both d_{shaft} =$\frac{d_0}{2}$ and $\frac{d_0}{3}$, while differences between d_{shaft} =$\frac{d_0}{2}$ and $\frac{d_0}{3}$ are not as striking. Moreover, the difference between d_{shaft} =d_0, $\frac{d_0}{2}$ and $\frac{d_0}{3}$ increases with τ_{IP3}. This suggests that geometries with d_{shaft} =d_0 better discriminate slow from fast frequency of node stimulation compared to geometries with thinner shafts. Geometries with d_{shaft} =d_0 are further characterized by a lower Ca^{2+} peak probability in node 5 compared to geometries with d_{shaft} =$\frac{d_0}{2}$ and $\frac{d_0}{3}$ (Fig 5B2). More precisely, Ca^{2+} peak probability decreases as τ_{IP3} increases for d_{shaft} =d_0, which was observed independently of our boundary conditions (Supplemental Fig 1, see Methods). This suggests that geometries with larger shafts could be associated with decreased signal propagation to remote nodes in case of repeated node stimulation at low frequency ($\tau_{\mathrm{IP3}} >$ 2s).

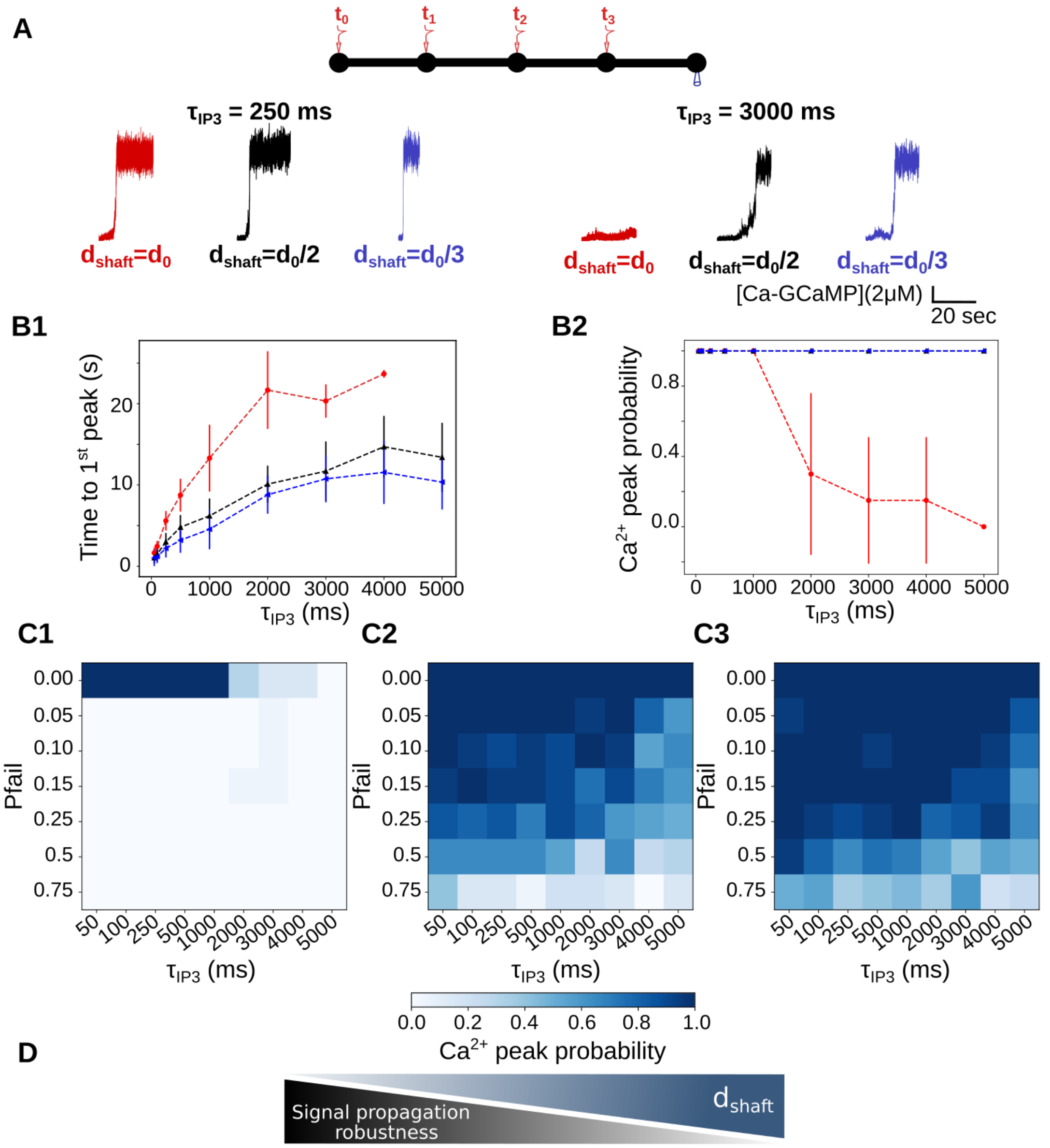

Figure 5. Thin shafts are associated with a more robust signal propagation upon repeated neuronal stimuli. (*A*) (*Top*) Neuronal stimulation protocol: node 1 is stimulated at t=t_0=5s, node 2 at $t_0 + \tau_{\mathrm{IP3}}$, node 3 at $t_0 + 2\tau_{\mathrm{IP3}}$ and node 4 at $t_0 + 3\tau_{\mathrm{IP3}}$, k_{Ca}=0 s^{-1}. Ca^{2+} activity is recorded in node 5. (*Bottom*) Representative Ca^{2+} traces in node 5 for shaft width $d_{\mathrm{shaft}} = d_0$ (red), $\frac{d_0}{2}$ (black) and $\frac{d_0}{3}$ (blue), with τ_{IP3}=250ms (left) and 3000ms (right), expressed as SNR (see Methods). (*B1*) Time to 1^{st} peak increases with τ_{IP3} for d_{shaft} =d_0 (***), $\frac{d_0}{2}$ (***) and $\frac{d_0}{3}$ (***). T-tests revealed that for any value of τ_{IP3}, time to 1^{st} peak is higher for d_{shaft} =d_0 compared to d_{shaft} =$\frac{d_0}{2}$ and $\frac{d_0}{3}$. Time to 1^{st} peak is significantly higher when d_{shaft} =$\frac{d_0}{2}$ compared to d_{shaft} =$\frac{d_0}{3}$, for most values of τ_{IP3} (p=0.032 *, 0.0025 **, 0.034 *, 0.016 * and 0.019 * for τ_{IP3}=250, 500, 1000, 4000 and 5000, respectively). (*B2*) Ca^{2+} peak probability in node 5 is lower for d_{shaft} =d_0 compared to d_{shaft} =$\frac{d_0}{2}$ and $\frac{d_0}{3}$. Ca^{2+} peak probability decreases as τ_{IP3} increases for d_{shaft} =d_0 (***). (*C*) Ca^{2+} peak probability in node 5 (colorbar) as a function of τ_{IP3} and of the probability of failure of node stimulation p_{fail}, for d_{shaft} =d_0 (C1), d_{shaft} =$\frac{d_0}{2}$ (C2) and d_{shaft} =$\frac{d_0}{3}$ (C3), with $p_{\mathrm{fail}} \in [0, 1]$. (*D*) Schematic summarizing the main conclusion of this figure: decreased shaft width allows signal propagation despite omitted node stimulation, thus favoring more robust signal propagation. Data are represented as mean ± STD, n=20 for each value of d_{shaft} and of τ_{IP3}. Lines in panel B are guides for the eyes. The effect of d_{shaft} on each Ca^{2+} signal characteristic was tested using one-way ANOVA. Significance is assigned by * for $p \leq 0.05$, ** for $p \leq 0.01$, *** for $p \leq 0.001$.

Figure 5–Figure supplement 1. Sensitivity study of the effect of boundary conditions on local Ca^{2+} activity upon repeated neuronal stimuli.

For τ_{IP3}=4s and $d_{\mathrm{shaft}} = \frac{d_0}{3}$, signals were detected in node 5 11.55 ± 3.89 s after the stimulation of node 1, which means that they occurred before the stimulation of node 4 (t=t_0 + 12s for τ_{IP3}=4s). This phenomenon was not observed for $d_{\mathrm{shaft}} = d_0$, for which time to 1^{st} peak when τ_{IP3}=4s was 23.67 ± 0.47 s. This suggests that for $d_{\mathrm{shaft}} = \frac{d_0}{3}$, contrary to $d_{\mathrm{shaft}} = d_0$, one node stimulation could be omitted without having any consequence on Ca^{2+} peak probability in node 5. In order to test this hypothesis, we have performed simulations in which the stimulation of nodes 2, 3 and 4 occurred with a given probability of failure p_{fail}. Simulations were performed for p_{fail}=0, 0.05, 0.1, 0.15, 0.25 and 0.75. Ca^{2+} peak probability in node 5, depending on p_{fail} and on τ_{IP3} is presented in Fig 5C, for $d_{\mathrm{shaft}} = d_0$ (Fig 5C1), $d_{\mathrm{shaft}} = \frac{d_0}{2}$ (Fig 5C2) and $d_{\mathrm{shaft}} = \frac{d_0}{3}$(Fig 5C3). As expected, Ca^{2+} peak probability, despite high values of p_{fail}, increases when d_{shaft} decreases. Thus, thin shafts can favor signal propagation by allowing the omission of a node stimulation. In that sense, geometries displaying thin shafts are characterized by a more robust signal propagation (Fig 5D).

Together, our results suggest that, in the context of repeated node stimulation, thin shafts are associated with an increase of Ca^{2+} peak probability in more remote nodes, with an earlier signal onset, suggesting increased signal propagation. Astrocytic processes with thicker shafts (here $d_{\mathrm{shaft}} = d_0$), such as observed in hypo-osmotic conditions (***Arizono et al., 2021b***), are associated with lower signal propagation in case of low stimulation frequency (time period > 2s), potentially favoring the formation of local Ca^{2+} hotspots. Our results suggest that geometries with thick shafts could impair signal propagation when a branchlet is stimulated at a low frequency. In that sense, astrocyte branchlets with thicker shafts would be better detectors of the surrounding level of neuronal activity. By contrast, branchlets with thin shafts would be less discriminating and provide more robust signal propagation.

Discussion

Fine astrocytic processes are responsible for most astrocytic Ca^{2+} signals (***Bindocci et al., 2017***) and are preferential sites of neuron-astrocyte communication (***Arizono et al., 2020***). A better understanding of the mechanistic link between their morphology and the spatio-temporal properties of local Ca^{2+} signals is crucial, yet hard to test experimentally. Here, we perform reaction-diffusion simulations in idealized morphologies of astrocytic processes derived from 3D super-resolution microscopy to investigate the effect of astrocyte nanoscale morphology on Ca^{2+} activity in the gliapil. Our simulation results suggest that the morphology of processes, alternating between large and thinner cellular compartments (***Panatier et al., 2014***; ***Arizono et al., 2020***; ***Grosche et al., 1999***), increases Ca^{2+} peak probability, duration, amplitude and propagation. Conversely, astrocyte swelling attenuates local Ca^{2+} activity and signal propagation (Fig 6). Our simulation results, in accordance with experimental data, suggest that thin shafts are associated with a decreased diffusion flux, i.e an increased compartmentalization of nodes. Thus, nodes, similarly to dendritic spines (***Santamaria et al., 2011***), act as diffusion traps when shaft width is low. Note that, more than the value of shaft width itself, our results emphasize the effect of the ratio between node and shaft diameter on Ca^{2+} activity. The geometries designed and used in this study emerge as interesting tools to investigate the influence of the ultrastructure of fine astrocyte branchlets on the local Ca^{2+} dynamics in health and disease. By recording the mechanisms resulting in Ca^{2+} signals upon neuronal stimulation in small cellular compartments of the gliapil, which cannot be performed experimentally, our simulation results shed light on the mechanisms by which astrocyte swelling influences the frequency, amplitude and propagation of Ca^{2+} signals at the nanoscale.

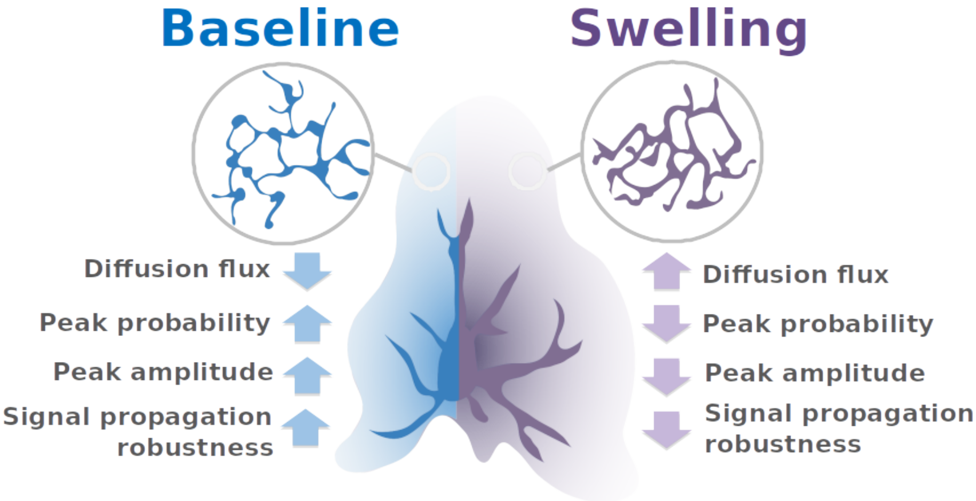

Figure 6. Proposed mechanisms that regulate astrocytic Ca^{2+} activity at tripartite synapses. Our simulation results demonstrate that the nano-morphology of astrocytic processes, consisting in the alternation of nodes and shafts, powerfully shapes the spatio-temporal properties of Ca^{2+} signals and promotes local Ca^{2+} activity. Astrocyte swelling, observed in pathological conditions such as brain injury, stroke and epilepsy, results in an increased shaft width without altering node size. Our results suggest that such pathological alterations of the nanoscale morphology of astrocytes result in a decreased local Ca^{2+} activity, which we confirm experimentally in hypo-osmotic conditions. Upon repeated neuronal stimuli, the we predict that swelling hinders astrocytic signal propagation. Overall, this study highlights the impact of astrocyte nano-morphology on astrocyte activity at tripartite synapses, in health and disease.

Experimental Ca^{2+} recordings of astrocyte activity have established that astrocyte processes display both highly localized microdomain signals and propagating Ca^{2+} waves (***Srinivasan et al., 2015***; ***Bindocci et al., 2017***). Our simulations suggest that the morphology of the cell and of its organelles can strongly influence the formation of these patterns of astrocytic Ca^{2+} signaling. Notably, thinner shafts allow less discriminating and more robust signal propagation upon repeated stimuli compared to larger shafts. Thinner shafts indeed allow signal propagation even in the absence of some stimuli or when the time interval between repeated stimuli is large. On the contrary, geometries with thick shafts seem to be more discriminating, potentially favoring the propagation of signals resulting from repeated stimuli from co-active synapses. Cellular morphology thus emerges as a key parameter that regulates the active propagation of Ca^{2+} signals. The ultrastructure of the spongiform domain of astrocytes is very complex, characterized by abundant branching points, conferring a reticular morphology (***Arizono et al., 2020***). Those branching points are reportedly sometimes arranged into ring-like structures, although their occurrence and shape are still debated and could differ depending on the brain region under study (***Arizono et al., 2020***; ***Panatier et al., 2014***; ***Kiyoshi et al., 2020***; ***Salmon et al., 2021***; ***Arizono and Nägerl, 2021***). The effect of this reticular ultrastructure on the propagation of Ca^{2+} signals remains to be uncovered. Further characterization of the shape of fine astrocytic processes of the spongiform domain, their variability as well as their connectivity to the neighboring synapses are thus required. Pairing those observations with biophysically-detailed models such as the one presented in this study stands to deepen our understanding of the roles of astrocytic and neuronal morphology at tripartite synapses on neuron-astrocyte communication.

In neurons, both experimental (***Yuste et al., 2000***; ***Noguchi et al., 2005***; ***Tønnesen et al., 2014***) and modelling (***Schmidt and Eilers, 2009***; ***Biess et al., 2007***; ***Simon et al., 2014***; ***Bell et al., 2019***; ***Holcman and Schuss, 2005***, ***2011***; ***Santamaria et al., 2011***; ***Cugno et al., 2019***) studies have suggested that thin spine necks favor the compartmentalization of Ca^{2+} signals within the spine head. This compartmentalization of synapses allows neurons to discriminate various inputs and to process information locally (***Wybo et al., 2019***; ***Poirazi and Papoutsi, 2020***), increasing the computational power of the neuronal circuits. According to our simulation results, nodes connected to thin shafts could favor the emergence of large signals at the site of neuron-astrocyte communication. Interestingly, we further propose that those amplified signals in nodes, instead of resulting in Ca^{2+} hotspots, favor active signal propagation. In response to spike timing-dependent plasticity (STDP) protocols (***Araya et al., 2014***) and after long-term potentiation (***Tønnesen et al., 2014***), the neck of dendritic spines become wider and shorter. Recent *in vitro* and *in vivo* studies have reported that the geometry of the ER in neurons is also highly dynamic (***Kucharz et al., 2013***), experiencing fast fission and fusion events. Further, the ER is variably distributed in spines, being preferentially present in large spines associated with strong synapses (***Holbro et al., 2009***). The geometries of dendrites and of their organelles, which influence local signals, are thus highly dynamic. Similarly, fine astrocytic processes encounter morphological rearrangements that are activity-dependent, which notably influence synaptic maturation, efficacy and spine stability (***Theodosis et al., 2008***; ***Zhou et al., 2019***; ***Henneberger et al., 2020***). Our study sheds light on the influence of rearrangements of the reticular morphology of fine processes on signal computation by astrocytes. Further investigation manipulating astrocyte morphology *in situ* as well as *in vivo* is required to better characterize the variability of astrocyte ultrastructure and the associated integration of Ca^{2+} signals.

The morphology of the complex spongiform domain of astrocytes is highly dynamic, subject to activity-dependent as well as pathological remodeling. Our study, providing mechanisms by which an altered astrocyte morphology influences neuron-astrocyte communication at the nanoscale, gives new insights into the involvement of astrocytes in brain function in health and disease.

Methods and Materials

Stochastic spatially-explicit voxel-based simulations

In order to model astrocyte Ca^{2+} signals in astrocyte branchlets, we have used the voxel-based "GCaMP" implementation of the Inositol 3-Phosphate (IP$_3$) receptor-dependent Ca^{2+} signaling model from Denizot et al (***Denizot et al., 2019a***), using the same reaction scheme and parameter values (Fig 1B). Briefly, we model Ca^{2+} fluxes in and out of the cytosol, mediated by Ca^{2+} channels and pumps on the endoplasmic reticulum (ER) and on the plasma membrane. Ca^{2+} signals occur when some IP$_3$R channels are in the open state. IP$_3$ can be synthesized by the Ca^{2+}-dependent activity of phospholipase C δ (PLCδ) and the removal of IP$_3$ molecules from the cytosol is expressed as a single decay rate. IP$_3$R kinetics is described by a Markov model, derived from De Young & Keizer's model (***De Young and Keizer, 1992***). Each IP$_3$R molecule contains one IP$_3$ binding site and two Ca^{2+} binding sites. An IP$_3$R is in the open state when in state $\{110\}$ (first Ca site and IP$_3$ bound, second Ca site free). Depending on the simulation, other diffusing molecules were added to the model, such as the fluorescent molecule ZsGreen and fluorescent Ca^{2+} indicators, here 10 μM of GCaMP6s. GCaMPs are genetically-encoded Ca^{2+} indicators (GECIs) that are derived from the fluorescent protein GFP and the Ca^{2+} buffer calmodulin (see (***Shigetomi et al., 2016***) for a review on GECIs). For further details on the kinetic scheme and model assumptions, please refer to Denizot et al. 2019 (***Denizot et al., 2019a***).

The model was implemented using STEPS (http://steps.sourceforge.net/), a python package performing exact stochastic simulation of reaction-diffusion systems (***Hepburn et al., 2012***). More presicely, STEPS uses a spatialized implementation of Gillespie's SSA algorithm (***Gillespie, 1977***; ***Isaacson and Isaacson, 2009***; ***Smith and Grima, 2018***). Simulations in STEPS can be performed in complex geometries in 3 spatial dimensions. Space is divided into well-mixed tetrahedral compartments, referred to as voxels. Reactions between 2 molecules can only occur if they are located within the same voxel. Diffusion events are modeled as a decrease of the number of molecules in the original voxel and an increase in the number of molecules in its neighboring voxel. Boundary conditions, except when specified otherwise, were reflective. In other words, mobile molecules could not diffuse away from the geometry, as if they were “bouncing” onto the plasma membrane. STEPS enables to compute, in complex 3D geometries, reactions and diffusion in the cytosol as well as reactions between cytosolic molecules and molecules located at the plasma or ER membrane.

Geometries

Typical astrocyte branchlet geometries were designed from their recent experimental characterization in live tissue at high spatial resolution (50 nm in x-y) (***Arizono et al., 2020***). Those geometries consist in alternations of bulbous structures, nodes, connected to each other with cylindrical structures, shafts. Geometries with different shaft widths d_{shaft} were designed using Trelis software (https://www.csimsoft.com/trelis, Fig 1A). The geometry of a node was approximated as being a sphere of diameter 380 nm. Shaft geometry consisted in a 1μm long cylinder. Shaft diameter was defined relative to node diameter. For example, shaft diameter was the same as node diameter, i.e d_{shaft} =d_0=380 nm. Similarly, shaft diameter was 190 nm and 127 nm for $d_{\text{shaft}} = \frac{d_0}{2}$ and $\frac{d_0}{3}$, respectively. Cones were positioned between spheres and cylinders in order to create a smoother transition between nodes and shafts, better approximating the geometry observed experimentally. Cytosolic volume was thus V_1=0.620 μm^3, V_2=0.263 μm^3 and V_3=0.195 μm^3, for d_{shaft} =d_0, $\frac{d_0}{2}$ and $\frac{d_0}{3}$, respectively. A subset of simulations were performed in a geometry with V_1=0.258 μm^3. This geometry is characterized, similarly to geometries with d_{shaft} =d_0, by a node/shaft width ratio of 1. It contains cylinders of length 750 nm, diameter 285 nm and spheres of diameter 285 nm. As a first approximation, ER geometry was considered to be similar to the geometry of the astrocyte branchlet: node/shaft successions. ER nodes were aligned with cytosolic nodes. As no quantification of the ER volume compared to cellular volume was found for astrocytes in the literature, ER volume was 10% of the total branchlet volume, based on available data in neurons (***Spacek and Harris, 1997***). The cytosolic volume, plasma and ER membrane areas of the different “5Nodes” geometries are presented in Table 1.

A sensitivity study was performed to investigate the effect of voxel size on the kinetics of the molecular interactions modeled. Information on the voxel sizes of the different meshes used is presented in Supplemental Table 1. Results are presented in Supplemental Fig 1. Meshes that contained voxels that were $<$ 50 nm^3 were characterized by aberrant kinetics, resulting in aberrant average numbers of molecules in a given state. Those results thus suggest that to prevent errors due to voxel size, meshes should not display voxel sizes that are$<$ 50 nm^3. We have thus made sure, while meshing the geometries in which simulations were ran, that no voxels were $<$ 50 nm^3. Minimum voxel size was 443 nm^3, 1100 nm^3 and 447 nm^3, for d_{shaft}=d_0, $\frac{d_0}{2}$ and $\frac{d_0}{3}$ geometries, respectively.

In a subset of simulations, ER geometry varied. The shape of the cell was the same as in “5nodes” geometries (Fig 1). ER geometry consisting of node/shaft alternations, described above, is referred to as “Node/shaft ER”. “No ER” geometry contains no ER. “Node ER” is characterized by a discontinuous ER geometry, consisting in spheres of diameter 54 nm, located in cellular nodes. “Cyl ER” corresponds to a cylindrical ER, of length l_{ER}= 6274 nm and a diameter of 108, 54 and 36 nm, for d_{shaft} =d_0, $\frac{d_0}{2}$ and $\frac{d_0}{3}$, respectively. The associated cytosolic volume, ER and plasma membrane area are presented in Table 1.

Protocol for simulating bleaching experiments

In order to test whether the idealized geometries presented in Fig 1 are a good approximation of the spongiform ultrastructure of astrocyte branchlets, we have simulated their fluorescence recovery after photobleaching (FRAP) experiments. Briefly, laser pulses are simulated on a node (region of interest) while the fluorescence level is being recorded. At bleaching time, the fluorescence level in the region of interest decreases to I_0. Then, because of the diffusion of fluorescent molecules into the region of interest, fluorescence increases until it reaches a new steady state, I_{inf}. We characterize node compartmentalization by measuring the time τ taken by fluorescing molecules to diffuse into the node to reach I_{inf}. In other words, a high node compartmentalization will be associated with a high value of τ. Thus, 3 main parameters characterize bleaching traces: I_0, τ and I_{inf}.

To mimic bleaching experiments in fine branchlets performed by Arizono et al (***Arizono et al., 2020***), ZsGreen molecules were added to simulation space. After 2 seconds of simulation, providing the basal level of fluorescence, 60% of ZsGreen molecules were bleached. In order to fit I_0 and I_{inf} that were measured experimentally, and as bleaching time lasted 10 ms in experiments and 1 ms in simulations, the bleached volume in simulations was adjusted depending on the geometry (see Fig 2A). Bleaching was simulated as a transition from ZsGreen molecules to ZsGreen-bleached molecules, the latter being considered as non-fluorescing molecules. Screenshots of simulations, illustrating the diffusion of ZsGreen and ZsGreen-bleached molecules, are presented in Fig S2B. The number of ZsGreen molecules in the central node was recorded over simulation time and a fit was performed following equation 1 to determine the values of I_0, I_{inf} and τ.

$$I(t) = I_0 - (I_0 - I_{\mathrm{inf}})e^{-\mathrm{t}/\tau} \tag{1}$$

, where I(t) is the level of fluorescence measured at time t. The coefficient of diffusion, D_{ZsGreen}, and the concentration, [ZsGreen], of ZsGreen were adjusted to fit experimental data. Indeed, the amplitude of [ZsGreen] fluctuations at steady state is inversely proportional to the number of ZsGreen molecules in the geometry. In other words, fluorescence signals are more noisy when [ZsGreen] is low. Moreover, the autocorrelation of those fluctuations depends on the coefficient of diffusion of ZsGreen, D_{ZsGreen}. If D_{ZsGreen} increases, the autocorrelation of Lag, where Lag is the autocorrelation delay, will decrease faster as Lag increases. Comparing the fluctuations of [ZsGreen] and its autocorrelation in experiments and in simulations thus enabled to find the values of D_{ZsGreen} and of [ZsGreen] that allowed for the best fit to experimental data. In the simulations presented here, D_{ZsGreen}=90 $\mu m^2.s^{-1}$ and [ZsGreen]=25 μM.

Protocols for simulating neuronal stimulation

In order to investigate the propagation of Ca^{2+} signals from nodes that contact neuronal spines, we have developed 2 different protocols for our simulations, performed in the geometries presented in Fig 1. As nodes were the site of Ca^{2+} signal initiation (***Arizono et al., 2020***) and as most spines contacted nodes rather than shafts, we have simulated neuronal stimulation in nodes. To simulate neuronal stimulation, IP_3 and Ca^{2+} were infused in the cytosol at stimulation time. IP_3 infusion reflects the production of IP_3 by phospholipase C that results from the activation of G_q-G-protein-coupled receptors (GPCRs). Ca^{2+} infusion mimics the influx of Ca^{2+} in the cytosol through Ca^{2+} channels at the plasma membrane. The rate of this neuronal activity-induced Ca^{2+} influx, k_{Ca}, varied within a physiological range of values, from 0 to 1000 s^{-1} (***Wu et al., 2018***; ***Brazhe et al., 2018***). Signals were recorded both in the stimulated node, Node 1, and in the neighboring node, Node 2.

- In the first protocol, 100 IP_3 molecules were infused in Node 1, at t=t_0=1s, while Ca^{2+} activity was monitored in Node 1 and in the neighboring node, Node 2 (see e.g Fig 3A). Neuronal activity-induced Ca^{2+} influx was mediated by generic Ca^{2+} channels at the plasma membrane. 25 of those Ca^{2+} channels were placed on the plasma membrane of Node 1, corresponding to a similar density to the IP_3R density on the ER membrane, and were set to an inactive state. At stimulation time t=t_0, Ca^{2+} channels were set to an active state, resulting in an influx of Ca^{2+} within the cytosol at rate k_{Ca}. At t=$t_0 + 1$, Ca^{2+} channels were set back to their initial inactive state. Simulations were performed in geometries with varying shaft width d_{shaft}.

- In the second protocol, we have investigated signal propagation in the node/shaft geometry depending on shaft width d_{shaft} when several nodes were successively stimulated. In "5nodes" geometries, 50 IP$_3$ molecules were infused at t_0=5s, $t_0 + \tau_{\mathrm{IP3}}$, $t_0 + 2\tau_{\mathrm{IP3}}$, $t_0 + 3\tau_{\mathrm{IP3}}$ in Nodes 1, 2, 3 and 4, respectively. During the whole simulation time, Ca^{2+} activity was recorded in Node 5 (see Fig 5). In a subset of simulations, stimulation of Nodes 2, 3 and 4 occurred with a probability $1 - p_{\mathrm{fail}}$, with $p_{\mathrm{fail}} \in [0, 1]$.

Peak detection and analysis

The same strategy as developed by Denizot et al. (***Denizot et al., 2019a***) was used for detecting and analysing Ca^{2+} signals. Briefly, basal concentration of Ca^{2+}, $[Ca]_{\mathrm{b}}$, was defined based on a histogram of the number of Ca^{2+} ions in the absence of neuronal stimulation. Peak initiation corresponded to the time when [Ca^{2+}] was higher than the following threshold: $[Ca]_{\mathrm{b}} + n\sigma_{\mathrm{Ca}}$, where σ_{Ca} is the standard deviation of [Ca^{2+}] histogram in the absence of neuronal stimulation. The value of n was set by hand depending on signal/noise ratio of the simulation of interest. Peak termination corresponded to the time when [Ca^{2+}] decreased below the peak threshold.
Several parameters were analyzed to characterize Ca^{2+} signals. Peak amplitude, A, corresponds to the maximum [Ca^{2+}] measured during the peak duration. It is expressed as signal to noise ratio $SNR = \frac{A-[Ca]_{\mathrm{b}}}{[Ca]_{\mathrm{b}}}$. Peak duration corresponds to the time between peak initiation and peak termination. Time to 1^{st} peak corresponds to the delay between the beginning of the simulation and the first peak detection, measured in the cellular compartment of interest. Peak probability corresponds to the fraction of simulations in which at least one peak was detected during simulation time in the region of interest. Ca^{2+} residency time was measured by performing n=300 simulations for each value of d_{shaft} , in which only 1 Ca^{2+} ion was added to node 1, without other molecular species. Ca^{2+} residency time corresponds to the time taken for the ion to diffuse away from node 1.

Organotypic hippocampal slice cultures

All experiments were performed as described in (***Arizono et al., 2020***) and were in accordance with the European Union and CNRS UMR5297 institutional guidelines for the care and use of laboratory animals (Council directive 2010/63/EU). Organotypic hippocampal slices (Gähwiler type) were dissected from 5–7-d-old wild-type mice and cultured 5–8 week in a roller drum at 35°C, as previously described (***Gähwiler, 1981***).

Viral infection

AAV9-GFAP-GCaMP6s (***Stobart et al., 2018b***) was injected by brief pressure pulses (40ms; 15 psi) into the stratum radiatum of 2-3-week old slices from Thy1-YFP-H (JAX:003782) mice 4-6 weeks prior to the experiment.

Image acquisition

For Ca^{2+} imaging, we used a custom-built setup based on an inverted microscope body (Leica DMI6000), as previously described in (***Tønnesen et al., 2011***). We used a 1.3 NA glycerol immersion objective equipped with a correction collar to reduce spherical aberrations and thereby allow imaging deeper inside brain tissue (***Urban et al., 2011***). The excitation light was provided by a pulsed diode laser (l = 485 nm, PicoQuant, Berlin, Germany). The fluorescence signal was confocally detected by an avalanche photodiode (APD; SPCM-AQRH-14-FC; PerkinElmer). The spatial resolution of the setup was around 175 nm (in x-y) and 450 nm (z). Confocal time-lapse imaging (12.5 x 25 μm, pixel size 100 nm) was performed at 2Hz for 2.5 min in artificial cerebrospinal fluid containing 125 mM NaCl, 2.5 mM KCl, 1.3 mM MgCl$_2$, 2 mM CaCl$_2$, 26 mM NaHCO$_3$, 1.25 mM NaH$_2$PO$_4$, 20 mM D-glucose, 1 mM Trolox; 300 mOsm; pH 7.4. Perfusion rate was 2 mL/min and the temperature 32

°C. Hypo-osmotic stress (300 mOsm to 200 mOsm) was applied by perfusing ACSF with reduced NaCl concentration (119 to 69 mM NaCl).

Quantification and statistical analysis

For each parameter set, 20 simulations, with different seeds, were generated. Each parameter describing Ca^{2+} dynamics was expressed as mean ± standard deviation. The effect of d_{shaft} on each Ca^{2+} signal characteristic was tested using one-way ANOVA. Comparison between two different conditions was performed using unpaired Student T-test if values followed a Gaussian distribution, Mann-Whitney test otherwise. Significance is assigned by * for $p \leq 0.05$, ** for $p \leq 0.01$, *** for $p \leq 0.001$.

Simulation code

The simulation code, implemented with STEPS 3.5.0, and the meshes are available on ModelDB (***McDougal et al., 2017***) at http://modeldb.yale.edu/266928, access code: lto42@tpk3D?. The original model from Denizot et al. (***Denizot et al., 2019a***) is available at http://modeldb.yale.edu/247694.

Acknowledgments

This work was funded by the Okinawa Institute of Science and Technology Graduate University and by JSPS (Japan Society for the Promotion of Science) Postdoctoral Fellowship for Research in Japan (Standard, P21733). We thank Iain Hepburn and Weiliang Chen of the Computational Neuroscience Unit, OIST, Okinawa, Japan for discussion about 3D meshes and STEPS.

References

Aboufares El Alaoui A, Jackson M, Fabri M, de Vivo L, Bellesi M. Characterization of Subcellular Organelles in Cortical Perisynaptic Astrocytes. Frontiers in Cellular Neuroscience. 2021; 14. https://www.frontiersin.org/articles/10.3389/fncel.2020.573944/full, doi: 10.3389/fncel.2020.573944, publisher: Frontiers.

Agarwal A, Wu PH, Hughes EG, Fukaya M, Tischfield MA, Langseth AJ, Wirtz D, Bergles DE. Transient Opening of the Mitochondrial Permeability Transition Pore Induces Microdomain Calcium Transients in Astrocyte Processes. Neuron. 2017 Feb; 93(3):587–605.e7. http://www.cell.com/neuron/abstract/S0896-6273(16)31007-8, doi: 10.1016/j.neuron.2016.12.034.

Ahmadpour N, Kantroo M, Stobart JL. Extracellular Calcium Influx Pathways in Astrocyte Calcium Microdomain Physiology. Biomolecules. 2021 Oct; 11(10):1467. https://www.mdpi.com/2218-273X/11/10/1467, doi: 10.3390/biom11101467, number: 10 Publisher: Multidisciplinary Digital Publishing Institute.

Araya R, Vogels TP, Yuste R. Activity-dependent dendritic spine neck changes are correlated with synaptic strength. Proceedings of the National Academy of Sciences. 2014 Jul; 111(28):E2895–E2904. https://www.pnas.org/content/111/28/E2895, doi: 10.1073/pnas.1321869111, publisher: National Academy of Sciences Section: PNAS Plus.

Arizono M, Bancelin S, Bethge P, Chéreau R, Idziak A, Inavalli VVGK, Pfeiffer T, Tønnesen J, Nägerl UV. Nanoscale imaging of the functional anatomy of the brain. Neuroforum. 2021 Mar; https://www.degruyter.com/document/doi/10.1515/nf-2021-0004/html, doi: 10.1515/nf-2021-0004, publisher: De Gruyter Section: Neuroforum.

Arizono M, Inavalli VVGK, Bancelin S, Fernández-Monreal M, Nägerl UV. Super-resolution shadow imaging reveals local remodeling of astrocytic microstructures and brain extracellular space after osmotic challenge. Glia. 2021; 69(6):1605–1613. https://onlinelibrary.wiley.com/doi/abs/10.1002/glia.23995, doi: 10.1002/glia.23995, _eprint: https://onlinelibrary.wiley.com/doi/pdf/10.1002/glia.23995.

Arizono M, Inavalli VVGK, Panatier A, Pfeiffer T, Angibaud J, Levet F, Veer MJTT, Stobart J, Bellocchio L, Mikoshiba K, Marsicano G, Weber B, Oliet SHR, Nägerl UV. Structural basis of astrocytic Ca 2+ signals at tripartite synapses. Nature Communications. 2020 Apr; 11(1):1–15. https://www.nature.com/articles/s41467-020-15648-4, doi: 10.1038/s41467-020-15648-4, number: 1 Publisher: Nature Publishing Group.

Arizono M, Nägerl UV. Deciphering the functional nano-anatomy of the tripartite synapse using stimulated emission depletion microscopy. Glia. 2021; n/a(n/a). https://onlinelibrary.wiley.com/doi/abs/10.1002/glia.24103, doi: 10.1002/glia.24103, _eprint: https://onlinelibrary.wiley.com/doi/pdf/10.1002/glia.24103.

Bartol TM, Keller DX, Kinney JP, Bajaj CL, Harris KM, Sejnowski TJ, Kennedy MB. Computational reconstitution of spine calcium transients from individual proteins. Frontiers in Synaptic Neuroscience. 2015 Oct; 7. https://www.ncbi.nlm.nih.gov/pmc/articles/PMC4595661/, doi: 10.3389/fnsyn.2015.00017.

Bell M, Bartol T, Sejnowski T, Rangamani P. Dendritic spine geometry and spine apparatus organization govern the spatiotemporal dynamics of calcium. The Journal of General Physiology. 2019 Aug; 151(8):1017–1034. http://jgp.rupress.org/content/151/8/1017, doi: 10.1085/jgp.201812261.

Bezprozvanny I, Watras J, Ehrlich BE. Bell-shaped calcium-response curves of Ins(1,4,5)P3- and calcium-gated channels from endoplasmic reticulum of cerebellum. Nature. 1991 Jun; 351(6329):751–754. doi: 10.1038/351751a0.

Biess A, Korkotian E, Holcman D. Diffusion in a dendritic spine: The role of geometry. Physical Review E. 2007 Aug; 76(2):021922. https://link.aps.org/doi/10.1103/PhysRevE.76.021922, doi: 10.1103/PhysRevE.76.021922, publisher: American Physical Society.

Bindocci E, Savtchouk I, Liaudet N, Becker D, Carriero G, Volterra A. Three-dimensional Ca^{2+} imaging advances understanding of astrocyte biology. Science. 2017 May; 356(6339):eaai8185. http://science.sciencemag.org/content/356/6339/eaai8185, doi: 10.1126/science.aai8185.

Brazhe AR, Postnov DE, Sosnovtseva O. Astrocyte calcium signaling: Interplay between structural and dynamical patterns. Chaos: An Interdisciplinary Journal of Nonlinear Science. 2018 Oct; 28(10):106320. https://aip.scitation.org/doi/abs/10.1063/1.5037153, doi: 10.1063/1.5037153.

Bushong EA, Martone ME, Jones YZ, Ellisman MH. Protoplasmic astrocytes in CA1 stratum radiatum occupy separate anatomical domains. The Journal of Neuroscience: The Official Journal of the Society for Neuroscience. 2002 Jan; 22(1):183–192.

Cali C, Agus M, Kare K, Boges DJ, Lehvaslaiho H, Hadwiger M, Magistretti PJ. 3D cellular reconstruction of cortical glia and parenchymal morphometric analysis from Serial Block-Face Electron Microscopy of juvenile rat. Progress in Neurobiology. 2019 Sep; p. 101696. http://www.sciencedirect.com/science/article/pii/S0301008219300139, doi: 10.1016/j.pneurobio.2019.101696.

Cugno A, Bartol TM, Sejnowski TJ, Iyengar R, Rangamani P. Geometric principles of second messenger dynamics in dendritic spines. Scientific Reports. 2019 Aug; 9(1):1–18. https://www.nature.com/articles/s41598-019-48028-0, doi: 10.1038/s41598-019-48028-0, number: 1 Publisher: Nature Publishing Group.

De Young GW, Keizer J. A single-pool inositol 1,4,5-trisphosphate-receptor-based model for agonist-stimulated oscillations in Ca2+ concentration. Proceedings of the National Academy of Sciences. 1992 Oct; 89(20):9895–9899. http://www.pnas.org/cgi/doi/10.1073/pnas.89.20.9895, doi: 10.1073/pnas.89.20.9895.

Denizot A, Arizono M, Nägerl UV, Soula H, Berry H. Simulation of calcium signaling in fine astrocytic processes: Effect of spatial properties on spontaneous activity. PLOS Computational Biology. 2019 Aug; 15(8):e1006795. https://journals.plos.org/ploscompbiol/article?id=10.1371/journal.pcbi.1006795, doi: 10.1371/journal.pcbi.1006795.

Denizot A, Berry H, Venugopal S. Computational Modeling of Intracellular Ca2+ Signals in Astrocytes. Encyclopedia of Computational Neuroscience. 2019; p. Submitted. Submitted.

Di Castro MA, Chuquet J, Liaudet N, Bhaukaurally K, Santello M, Bouvier D, Tiret P, Volterra A. Local Ca2+ detection and modulation of synaptic release by astrocytes. Nature Neuroscience. 2011 Oct; 14(10):1276–1284. doi: 10.1038/nn.2929.

Giaume C, Venance L. Intercellular calcium signaling and gap junctional communication in astrocytes. Glia. 1998 Sep; 24(1):50–64. http://onlinelibrary.wiley.com.insb.bib.cnrs.fr/doi/10.1002/(SICI)1098-1136(199809)24:1<50::AID-GLIA6>3.0.CO;2-4/abstract, doi: 10.1002/(SICI)1098-1136(199809)24:1<50::AID-GLIA6>3.0.CO;2-4.

Gillespie DT. Exact stochastic simulation of coupled chemical reactions. The Journal of Physical Chemistry. 1977 Dec; 81(25):2340–2361. https://doi.org/10.1021/j100540a008, doi: 10.1021/j100540a008.

Grosche J, Matyash V, Möller T, Verkhratsky A, Reichenbach A, Kettenmann H. Microdomains for neuron–glia interaction: parallel fiber signaling to Bergmann glial cells. Nature Neuroscience. 1999 Feb; 2(2):139–143. https://www.nature.com/articles/nn0299_139, doi: 10.1038/5692.

Gähwiler BH. Organotypic monolayer cultures of nervous tissue. Journal of Neuroscience Methods. 1981 Dec; 4(4):329–342. http://www.sciencedirect.com/science/article/pii/0165027081900030, doi: 10.1016/0165-0270(81)90003-0.

Haustein MD, Kracun S, Lu XH, Shih T, Jackson-Weaver O, Tong X, Xu J, Yang XW, O'Dell TJ, Marvin JS, Ellisman MH, Bushong EA, Looger LL, Khakh BS. Conditions and constraints for astrocyte calcium signaling in the hippocampal mossy fiber pathway. Neuron. 2014 Apr; 82(2):413–429. doi: 10.1016/j.neuron.2014.02.041.

Henneberger C, Bard L, Panatier A, Reynolds JP, Kopach O, Medvedev NI, Minge D, Herde MK, Anders S, Kraev I, Heller JP, Rama S, Zheng K, Jensen TP, Sanchez-Romero I, Jackson CJ, Janovjak H, Ottersen OP, Nagelhus EA, Oliet SHR, et al. LTP Induction Boosts Glutamate Spillover by Driving Withdrawal of Perisynaptic Astroglia. Neuron. 2020 Sep; http://www.sciencedirect.com/science/article/pii/S0896627320306619, doi: 10.1016/j.neuron.2020.08.030.

Hepburn I, Chen W, Wils S, De Schutter E. STEPS: efficient simulation of stochastic reaction–diffusion models in realistic morphologies. BMC Systems Biology. 2012; 6(1):36. http://bmcsystbiol.biomedcentral.com/articles/10.1186/1752-0509-6-36, doi: 10.1186/1752-0509-6-36.

Holbro N, Grunditz A, Oertner TG. Differential distribution of endoplasmic reticulum controls metabotropic signaling and plasticity at hippocampal synapses. Proceedings of the National Academy of Sciences. 2009 Sep; 106(35):15055–15060. https://www.pnas.org/content/106/35/15055, doi: 10.1073/pnas.0905110106, publisher: National Academy of Sciences Section: Biological Sciences.

Holcman D, Schuss Z. Modeling Calcium Dynamics in Dendritic Spines. SIAM Journal on Applied Mathematics. 2005 Jan; 65(3):1006–1026. https://epubs.siam.org/doi/abs/10.1137/S003613990342894X, doi: 10.1137/S003613990342894X.

Holcman D, Schuss Z. Diffusion laws in dendritic spines. The Journal of Mathematical Neuroscience. 2011 Oct; 1(1):10. https://doi.org/10.1186/2190-8567-1-10, doi: 10.1186/2190-8567-1-10.

Isaacson SA, Isaacson D. The Reaction-Diffusion Master Equation, Diffusion Limited Reactions, and Singular Potentials. Physical Review E, Statistical, Nonlinear, and Soft Matter Physics. 2009 Dec; 80(6 Pt 2):066106. http://www.ncbi.nlm.nih.gov/pmc/articles/PMC3405976/.

Kiyoshi CM, Aten S, Arzola EP, Patterson JA, Taylor AT, Du Y, Guiher AM, Philip M, Camacho EG, Mediratta D, Collins K, Benson E, Kidd G, Terman D, Zhou M. Ultrastructural view of astrocyte-astrocyte and astrocyte-synapse contacts within the hippocampus; 2020.

Kucharz K, Wieloch T, Toresson H. Fission and Fusion of the Neuronal Endoplasmic Reticulum. Translational Stroke Research. 2013 Dec; 4(6):652–662. https://link.springer.com/article/10.1007/s12975-013-0279-9, doi: 10.1007/s12975-013-0279-9.

Lafrenaye AD, Simard JM. Bursting at the Seams: Molecular Mechanisms Mediating Astrocyte Swelling. International Journal of Molecular Sciences. 2019 Jan; 20(2):330. https://www.mdpi.com/1422-0067/20/2/330, doi: 10.3390/ijms20020330, number: 2 Publisher: Multidisciplinary Digital Publishing Institute.

Lind BL, Brazhe AR, Jessen SB, Tan FCC, Lauritzen MJ. Rapid stimulus-evoked astrocyte Ca2+ elevations and hemodynamic responses in mouse somatosensory cortex in vivo. Proceedings of the National Academy of Sciences. 2013 Nov; p. 201310065. http://www.pnas.org/content/early/2013/11/08/1310065110, doi: 10.1073/pnas.1310065110.

Majewska A, Brown E, Ross J, Yuste R. Mechanisms of Calcium Decay Kinetics in Hippocampal Spines: Role of Spine Calcium Pumps and Calcium Diffusion through the Spine Neck in Biochemical Compartmentalization. Journal of Neuroscience. 2000 Mar; 20(5):1722–1734. http://www.jneurosci.org/content/20/5/1722, doi: 10.1523/JNEUROSCI.20-05-01722.2000.

McDougal RA, Morse TM, Carnevale T, Marenco L, Wang R, Migliore M, Miller PL, Shepherd GM, Hines ML. Twenty years of ModelDB and beyond: building essential modeling tools for the future of neuroscience. Journal of Computational Neuroscience. 2017 Feb; 42(1):1–10. doi: 10.1007/s10827-016-0623-7.

Noguchi J, Matsuzaki M, Ellis-Davies GCR, Kasai H. Spine-Neck Geometry Determines NMDA Receptor-Dependent Ca2+ Signaling in Dendrites. Neuron. 2005 May; 46(4):609–622. http://www.sciencedirect.com/science/article/pii/S0896627305002382, doi: 10.1016/j.neuron.2005.03.015.

Oberheim NA, Wang X, Goldman S, Nedergaard M. Astrocytic complexity distinguishes the human brain. Trends in Neurosciences. 2006 Oct; 29(10):547–553. doi: 10.1016/j.tins.2006.08.004.

Otsu Y, Couchman K, Lyons DG, Collot M, Agarwal A, Mallet JM, Pfrieger FW, Bergles DE, Charpak S. Calcium dynamics in astrocyte processes during neurovascular coupling. Nature Neuroscience. 2015 Feb; 18(2):210–218. http://www.nature.com/neuro/journal/v18/n2/full/nn.3906.html, doi: 10.1038/nn.3906.

Panatier A, Arizono M, Nägerl UV. Dissecting tripartite synapses with STED microscopy. Phil Trans R Soc B. 2014 Oct; 369(1654):20130597. http://rstb.royalsocietypublishing.org/content/369/1654/20130597, doi: 10.1098/rstb.2013.0597.

Panatier A, Vallée J, Haber M, Murai KK, Lacaille JC, Robitaille R. Astrocytes are endogenous regulators of basal transmission at central synapses. Cell. 2011 Sep; 146(5):785–798. doi: 10.1016/j.cell.2011.07.022.

Poirazi P, Papoutsi A. Illuminating dendritic function with computational models. Nature Reviews Neuroscience. 2020 Jun; 21(6):303–321. https://www.nature.com/articles/s41583-020-0301-7, doi: 10.1038/s41583-020-0301-7, number: 6 Publisher: Nature Publishing Group.

Reichenbach A, Derouiche A, Kirchhoff F. Morphology and dynamics of perisynaptic glia. Brain Research Reviews. 2010 May; 63(1-2):11–25. doi: 10.1016/j.brainresrev.2010.02.003.

Rusakov DA. Disentangling calcium-driven astrocyte physiology. Nature Reviews Neuroscience. 2015 Apr; 16(4):226–233. http://www.nature.com/nrn/journal/v16/n4/full/nrn3878.html, doi: 10.1038/nrn3878.

Salmon CK, Syed TA, Kacerovsky JB, Alivodej N, Schober AL, Pratte MT, Rosen MP, Green M, Chirgwin-Dasgupta A, Vali H, Mandato CA, Siddiqi K, Murai KK. Organizing Principles of Astrocytic Nanoarchitecture in the Mouse Cerebral Cortex; 2021.

Santamaria F, Wils S, De Schutter E, Augustine GJ. The diffusional properties of dendrites depend on the density of dendritic spines. The European Journal of Neuroscience. 2011 Aug; 34(4):561–568. doi: 10.1111/j.1460-9568.2011.07785.x.

Schmidt H, Eilers J. Spine neck geometry determines spino-dendritic cross-talk in the presence of mobile endogenous calcium binding proteins. Journal of Computational Neuroscience. 2009 Oct; 27(2):229–243. https://doi.org/10.1007/s10827-009-0139-5, doi: 10.1007/s10827-009-0139-5.

Schuss Z, Singer A, Holcman D. The narrow escape problem for diffusion in cellular microdomains. Proceedings of the National Academy of Sciences. 2007 Oct; 104(41):16098–16103. https://www.pnas.org/content/104/41/16098, doi: 10.1073/pnas.0706599104, publisher: National Academy of Sciences Section: Physical Sciences.

Semyanov A, Henneberger C, Agarwal A. Making sense of astrocytic calcium signals — from acquisition to interpretation. Nature Reviews Neuroscience. 2020 Sep; p. 1–14. https://www.nature.com/articles/s41583-020-0361-8, doi: 10.1038/s41583-020-0361-8, publisher: Nature Publishing Group.

Sherwood MW, Arizono M, Hisatsune C, Bannai H, Ebisui E, Sherwood JL, Panatier A, Oliet SHR, Mikoshiba K. Astrocytic IP3Rs: Contribution to Ca2+ signalling and hippocampal LTP. Glia. 2017 Mar; 65(3):502–513. http://onlinelibrary.wiley.com/doi/10.1002/glia.23107/abstract, doi: 10.1002/glia.23107.

Shigetomi E, Bushong EA, Haustein MD, Tong X, Jackson-Weaver O, Kracun S, Xu J, Sofroniew MV, Ellisman MH, Khakh BS. Imaging calcium microdomains within entire astrocyte territories and endfeet with GCaMPs expressed using adeno-associated viruses. The Journal of General Physiology. 2013 May; 141(5):633–647. doi: 10.1085/jgp.201210949.

Shigetomi E, Patel S, Khakh BS. Probing the Complexities of Astrocyte Calcium Signaling. Trends in Cell Biology. 2016 Apr; 26(4):300–312. doi: 10.1016/j.tcb.2016.01.003.

Shigetomi E, Saito K, Sano F, Koizumi S. Aberrant Calcium Signals in Reactive Astrocytes: A Key Process in Neurological Disorders. International Journal of Molecular Sciences. 2019 Jan; 20(4):996. https://www.mdpi.com/1422-0067/20/4/996, doi: 10.3390/ijms20040996.

Simon CM, Hepburn I, Chen W, Schutter ED. The role of dendritic spine morphology in the compartmentalization and delivery of surface receptors. Journal of Computational Neuroscience. 2014 Jun; 36(3):483–497. https://link.springer.com/article/10.1007/s10827-013-0482-4, doi: 10.1007/s10827-013-0482-4.

Smith S, Grima R. Spatial Stochastic Intracellular Kinetics: A Review of Modelling Approaches. Bulletin of Mathematical Biology. 2018 May; https://doi.org/10.1007/s11538-018-0443-1, doi: 10.1007/s11538-018-0443-1.

Spacek J, Harris KM. Three-Dimensional Organization of Smooth Endoplasmic Reticulum in Hippocampal CA1 Dendrites and Dendritic Spines of the Immature and Mature Rat. Journal of Neuroscience. 1997 Jan; 17(1):190–203. http://www.jneurosci.org/content/17/1/190, doi: 10.1523/JNEUROSCI.17-01-00190.1997.

Srinivasan R, Huang BS, Venugopal S, Johnston AD, Chai H, Zeng H, Golshani P, Khakh BS. Ca(2+) signaling in astrocytes from Ip3r2(-/-) mice in brain slices and during startle responses in vivo. Nature Neuroscience. 2015 May; 18(5):708–717. doi: 10.1038/nn.4001.

Stobart JL, Ferrari KD, Barrett MJP, Glück C, Stobart MJ, Zuend M, Weber B. Cortical Circuit Activity Evokes Rapid Astrocyte Calcium Signals on a Similar Timescale to Neurons. Neuron. 2018 May; 98(4):726–735.e4. http://www.sciencedirect.com/science/article/pii/S0896627318302848, doi: 10.1016/j.neuron.2018.03.050.

Stobart JL, Ferrari KD, Barrett MJP, Stobart MJ, Looser ZJ, Saab AS, Weber B. Long-term In Vivo Calcium Imaging of Astrocytes Reveals Distinct Cellular Compartment Responses to Sensory Stimulation. Cerebral Cortex (New York, NY: 1991). 2018 Jan; 28(1):184–198. doi: 10.1093/cercor/bhw366.

Theodosis DT, Poulain DA, Oliet SHR. Activity-dependent structural and functional plasticity of astrocyte-neuron interactions. Physiological Reviews. 2008 Jul; 88(3):983–1008. doi: 10.1152/physrev.00036.2007.

Tønnesen J, Katona G, Rózsa B, Nägerl UV. Spine neck plasticity regulates compartmentalization of synapses. Nature Neuroscience. 2014 May; 17(5):678–685. https://www.nature.com/articles/nn.3682, doi: 10.1038/nn.3682, number: 5 Publisher: Nature Publishing Group.

Tønnesen J, Nadrigny F, Willig K, Wedlich-Söldner R, Nägerl UV. Two-Color STED Microscopy of Living Synapses Using A Single Laser-Beam Pair. Biophysical Journal. 2011 Nov; 101(10):2545–2552. http://www.sciencedirect.com/science/article/pii/S0006349511012008, doi: 10.1016/j.bpj.2011.10.011.

Urban N, Willig K, Hell S, Nägerl UV. STED Nanoscopy of Actin Dynamics in Synapses Deep Inside Living Brain Slices. Biophysical Journal. 2011 Sep; 101(5):1277–1284. http://www.sciencedirect.com/science/article/pii/S000634951100885X, doi: 10.1016/j.bpj.2011.07.027.

Verkhratsky A, Nedergaard M. Physiology of Astroglia. Physiological Reviews. 2018 Jan; 98(1):239–389. doi: 10.1152/physrev.00042.2016.

Witcher MR, Kirov SA, Harris KM. Plasticity of perisynaptic astroglia during synaptogenesis in the mature rat hippocampus. Glia. 2007 Jan; 55(1):13–23. doi: 10.1002/glia.20415.

Wu YW, Gordleeva S, Tang X, Shih PY, Dembitskaya Y, Semyanov A. Morphological profile determines the frequency of spontaneous calcium events in astrocytic processes. bioRxiv. 2018 Sep; p. 410076. https://www.biorxiv.org/content/early/2018/09/06/410076, doi: 10.1101/410076.

Wybo WAM, Torben-Nielsen B, Nevian T, Gewaltig MO. Electrical Compartmentalization in Neurons. Cell Reports. 2019 Feb; 26(7):1759–1773.e7. https://www.sciencedirect.com/science/article/pii/S2211124719301032, doi: 10.1016/j.celrep.2019.01.074.

Yasuda R. Biophysics of Biochemical Signaling in Dendritic Spines: Implications in Synaptic Plasticity. Biophysical Journal. 2017 Nov; 113(10):2152–2159. http://www.sciencedirect.com/science/article/pii/S000634951730855X, doi: 10.1016/j.bpj.2017.07.029.

Yuste R, Majewska A, Holthoff K. From form to function: calcium compartmentalization in dendritic spines. Nature Neuroscience. 2000 Jul; 3(7):653–659. doi: 10.1038/76609.

Zhou B, Zuo YX, Jiang RT. Astrocyte morphology: Diversity, plasticity, and role in neurological diseases. CNS neuroscience & therapeutics. 2019 Mar; doi: 10.1111/cns.13123.

Table 2. Characteristics of meshes used to investigate the effect of voxel size on Ca^{2+} signals. Cylinder geometries were generated with various total number of tetrahedra (geometry Cyl_i with $i \in [1,8]$, see also Fig 1A), resulting in different voxel sizes. V_{mean} corresponds to the average voxel volume, V_{std} to its standard deviation, V_{max} to the maximum voxel volume and V_{min} to the minimum voxel volume in the mesh. Volumes are expressed in nm^3. Diff (nm^3) corresponds to $V_{\text{max}} - V_{\text{min}}$ while Diff (%) is the ratio $\frac{V_{\text{max}} - V_{\text{min}}}{V_{\text{mean}}} * 100$

Geom	# tet	V_{mean}	V_{std}	V_{max}	V_{min}	Diff (nm^3)	Diff (%)
Cyl_1	372148	84	25	296	15	281	335
Cyl_2	274233	115	34	389	20	369	321
Cyl_3	125927	249	71	761	33	728	292
Cyl_4	40077	782	229	2200	67	2133	273
Cyl_5	11523	2700	790	7521	177	7344	272
Cyl_6	3103	9900	3200	24000	94	23906	241
Cyl_7	1417	21000	11000	62000	241	61759	294
Cyl_8	945	32000	28000	145000	241	144759	452

Supplemental Movie 1

Movie presenting a simulation of the bleaching protocol, with $d_{\text{shaft}}=\frac{d_0}{2}$. Fluorescing ZsGreen molecules are in red and bleached, non-fluorescing, ZsGreen are in yellow. Molecule position was updated every 1 ms. The plot presents the variation of the number of fluorescing ZsGreen molecules with time in the central node. Note that, to facilitate visualization, here [ZsGreen] = 5 μM. Before the bleaching event, all ZsGreen proteins (red) fluoresce. At bleaching time, fluorescing molecules in the bleached region encounter conformational modifications that prevent them from fluorescing (yellow molecules). Consequently, the fluorescence level drops to I_0. Because of the diffusion of molecules in the cell, the fluorescence level in the central node then increases until it reaches a new baseline I_{inf}, after a recovery time τ. Fluorescing ZsGreen molecules are in red and bleached, non-fluorescing, ZsGreen are in yellow.

Supplemental Movie 2

Movie presenting a simulation of the neuronal stimulation protocol, with $d_{\text{shaft}}=\frac{d_0}{2}$ and Ca^{2+} influx rate at the plasma membrane k_{Ca}=0 s^{-1}. 100 IP_3 molecules are injected in Node 1 at t=t_0=0.1s, while the number of Ca-GCaMP, IP_3 and IP_3R channels in the open state are monitored in nodes 1 and 2. Molecule position was updated every 0.1 ms. Ca-GCaMP molecules are in yellow, IP_3 in red and IP_3R in blue. Note that the size of molecules in the movie was increased to facilitate visualization. Speed was increased 5-fold for visualization purposes.

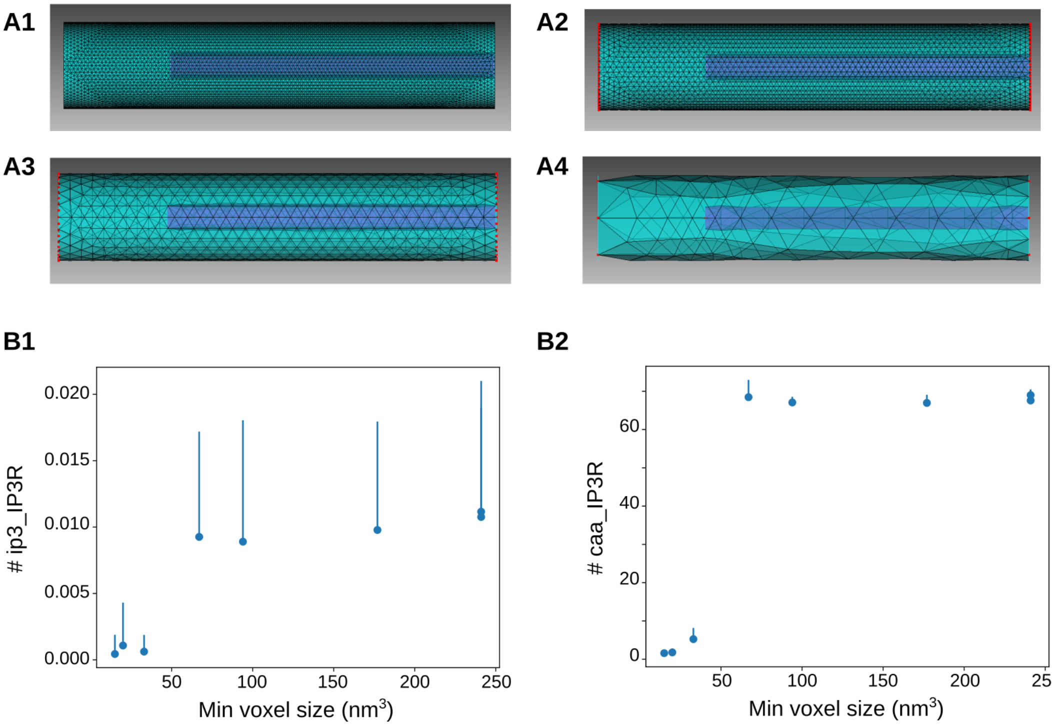

Figure 1–Figure supplement 1. Sensitivity study of the effect of voxel size on Ca^{2+} signals. (*A*) Simulations were performed in a cylinder geometry with various numbers of tetrahedra. 4 examples are presented here, “Cyl_1” (A1), “Cyl_3” (A2), “Cyl_5” (A3) and “Cyl_8” (A4). Please refer to Table 2 for details on the characteristics of each mesh. (B) Study of the average number of IP3R in the ip3_IP3R state (IP$_3$ bound to its binding site on IP$_3$R, B1) and in the caa_IP3R state (Ca^{2+} bound to the activating site of IP$_3$R, B2) depending on the mimimum voxel size of the mesh.

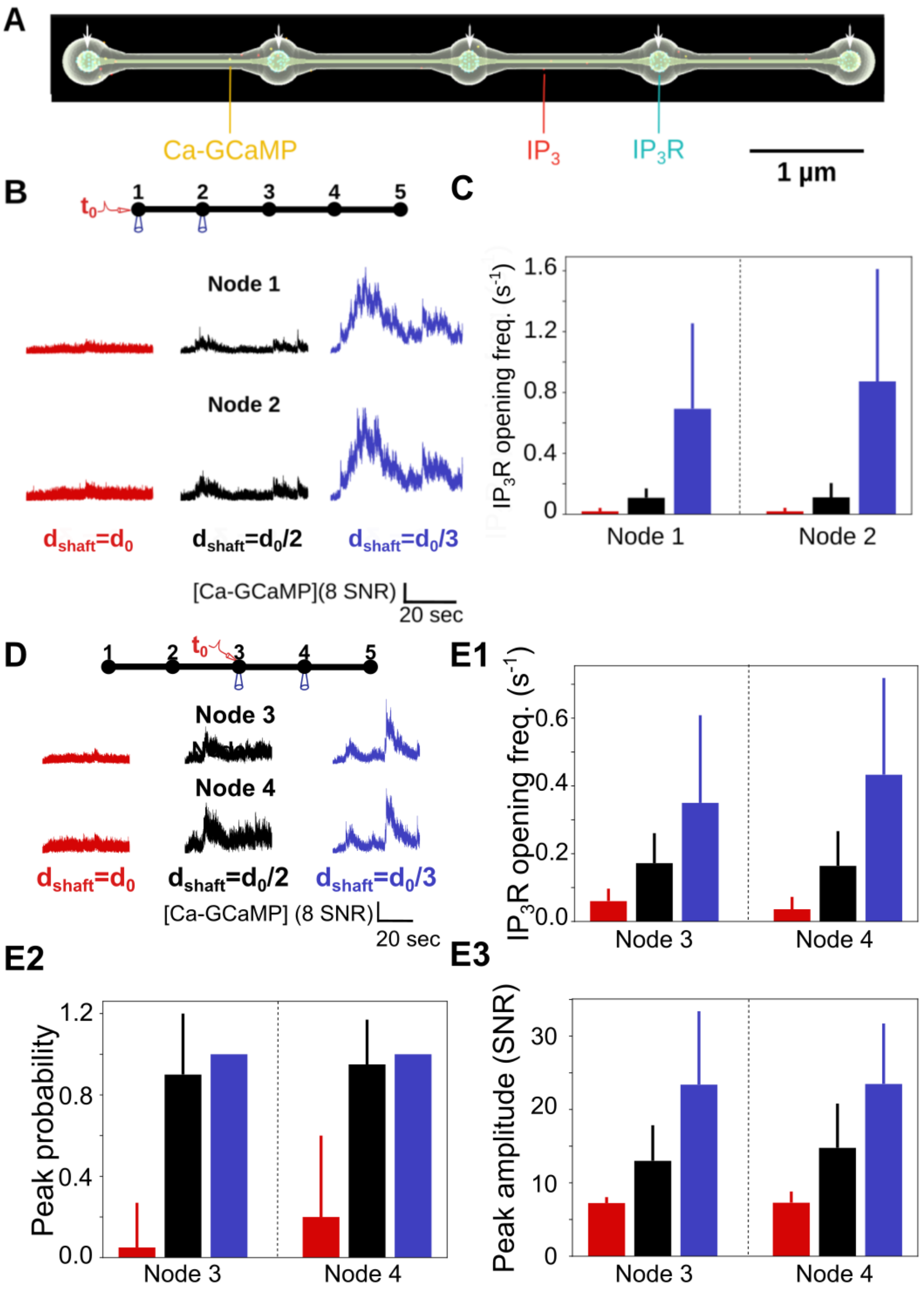

Figure 3–Figure supplement 1. Sensitivity study of the effect of shaft width on local Ca^{2+} signals upon single node stimulation. (*A*) Screenshot of a simulation in the "5nodes" $d_{\mathrm{shaft}} = \frac{d_0}{3}$ geometry. In those simulations, IP$_3$Rs are only positioned on the ER membrane in nodes (white arrows). The number of IP$_3$R channels is 300 for all values of d_{shaft}. (*B*) (*Top*) Node 1 was stimulated at t=t_0=1s, while Ca^{2+} activity was monitored in nodes 1 and 2. (*Bottom*) Representative Ca^{2+} traces in node 1 and node 2 for d_{shaft}=d_0 (red), $\frac{d_0}{2}$ (black) and $\frac{d_0}{3}$ (blue). (*C*) The frequency of IP$_3$R opening increases with d_{shaft} decreases in nodes 1 (***) and 2 (***). (*D*) (*Top*) In a second set of simulations, node 3 was stimulated at t=t_0=1s (k_{Ca}=0 s^{-1}), while Ca^{2+} activity was monitored in nodes 3 and 4. (*Bottom*) Representative [Ca-GCaMP] traces in nodes 3 and 4, expressed as SNR (see Methods), for d_{shaft}=d_0 (red), $\frac{d_0}{2}$ (black) and $\frac{d_0}{3}$ (blue). (*E1*) The frequency of IP$_3$R opening increases when d_{shaft} decreases in node 3 (***) and 4 (***). (*E2*) Ca^{2+} peak probability increases when d_{shaft} decreases in node 3 (***) and 4 (***). (*E3*) Peak amplitude increases when d_{shaft} decreases in node 3 (***) and 4 (***). Data are represented as mean ± STD, n=20 for each geometry. The effect of d_{shaft} on each Ca^{2+} signal characteristic was tested using one-way ANOVA. Significance is assigned by * for $p \leq 0.05$, ** for $p \leq 0.01$, *** for $p \leq 0.001$.

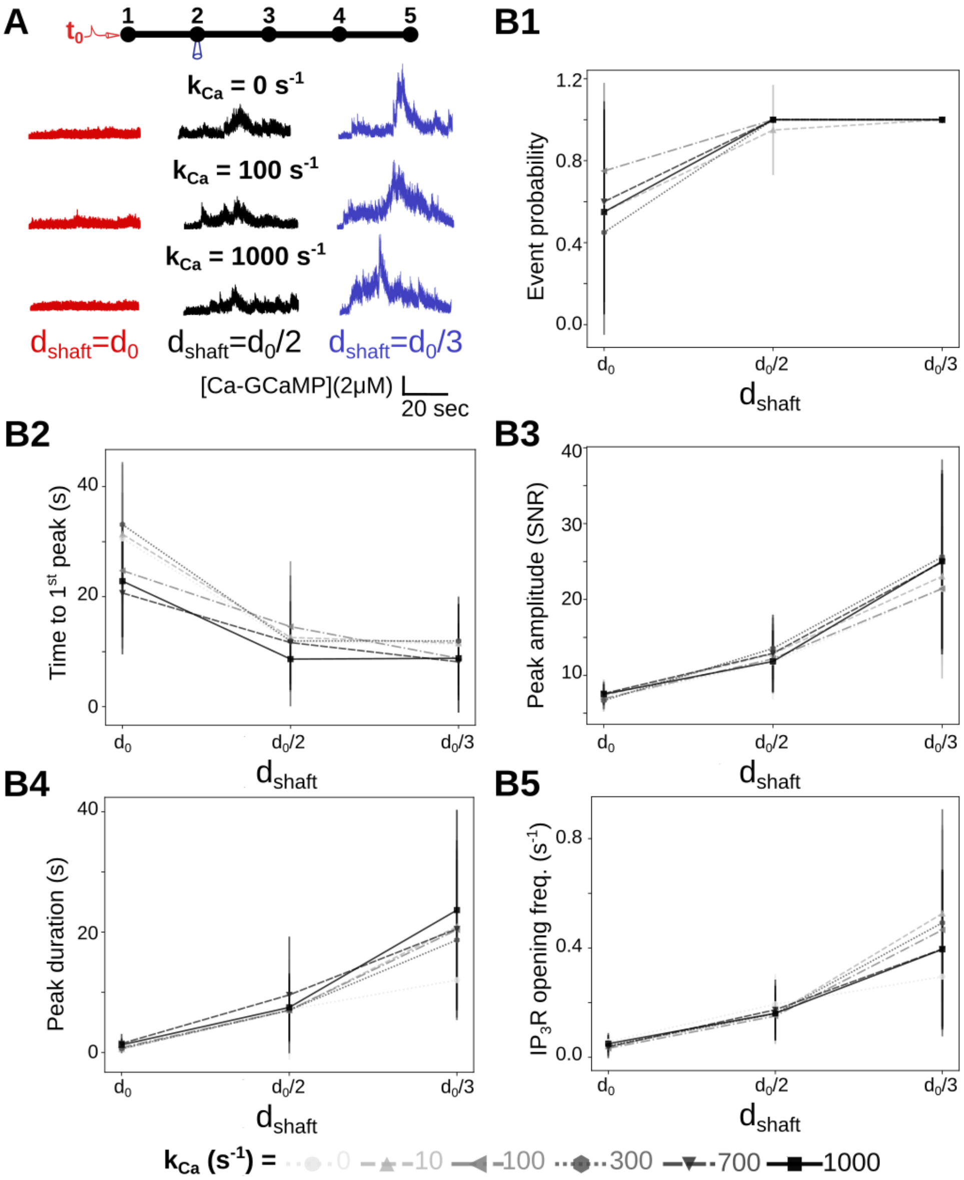

Figure 3–Figure supplement 2. Effect of Ca^{2+} influx rate at the plasma membrane on local Ca^{2+} signals. *A*) (*Top*) Neuronal stimulation protocol simulated for each geometry: node 1 was stimulated at t=t_0=1s, while Ca^{2+} activity was monitored in node 2. Representative Ca^{2+} traces for shaft width $d_{\mathrm{shaft}} = d_0$ (red), $\frac{d_0}{2}$ (black) and $\frac{d_0}{3}$ (blue), with a Ca^{2+} influx rate at the plasma membrane k_{Ca}=0 (top), 100 (middle) and 1000 s^{-1} (bottom), expressed as SNR (see Methods). (*B*) Quantification of the effect of d_{shaft} on Ca^{2+} signal characteristics for k_{Ca}=0, 10, 100, 300, 700 and 1000 s^{-1}. Data are represented as mean ± STD, n=20 for each set of parameters tested. Ca^{2+} peak probability increases (***, *B1*), Time to 1^{st} peak decreases (***, *B2*), peak amplitude (***, *B3*) and duration (***, *B4*) increase when d_{shaft} decreases, for k_{Ca}=0, 10, 100, 300, 700 and 1000 s^{-1}. Ca^{2+} peak characteristics did not statistically vary with k_{Ca}. The effect of k_{Ca} on each Ca^{2+} signal characteristic was tested using one-way ANOVA.

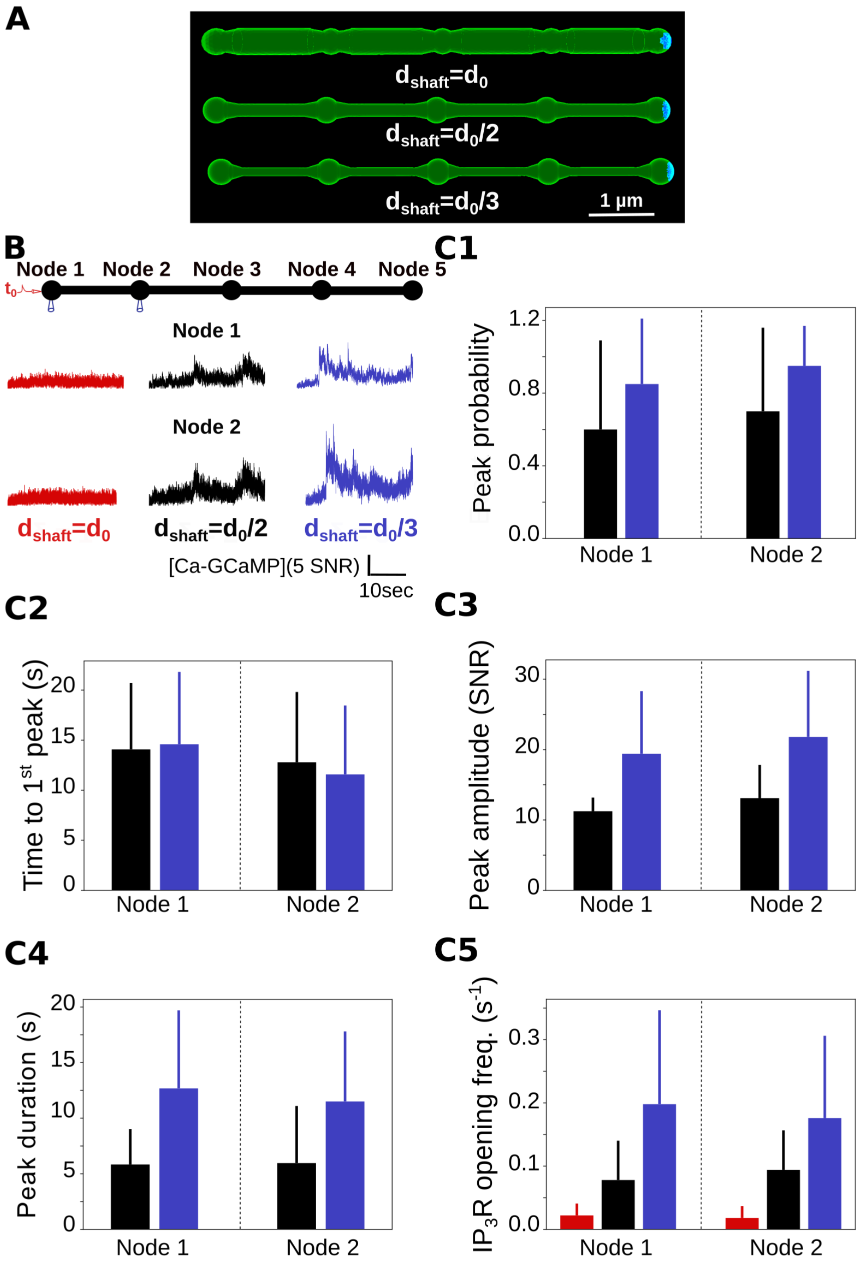

Figure 3–Figure supplement 3. Sensitivity study of the effect of boundary conditions on local Ca^{2+} activity upon single node stimulation. (*A*) Geometries used in the simulations were the “5nodes” geometries (Fig 1A). Boundary conditions were absorbing at the extremity of node 5 (blue), while the remaining boundaries were reflective (green). This mimics the connection of the modeled astrocyte branchlet to the rest of the cell. (*B*) (*Top*) Neuronal stimulation protocol simulated for each geometry: node 1 was stimulated at t=t_0=1s (k_{Ca}=0 s^{-1}), while Ca^{2+} activity was monitored in nodes 1 and 2. (*Bottom*) Representative [Ca-GCaMP] traces in nodes 1 and 2, expressed as SNR (see Methods), for d_{shaft}=d_0 (red), $\frac{d_0}{2}$ (black) and $\frac{d_0}{3}$ (blue). (*C1*) Ca^{2+} peak probability increases when d_{shaft} decreases in nodes 1 (***) and 2 (***). (*C2*) Time to 1^{st} peak does not change with d_{shaft}, both in node 1 (p-value=0.85) and 2 (p-value=0.90). (*C3*) Peak amplitude increases when d_{shaft} decreases in nodes 1 (p-value=0.0056 **) and 2 (p-value=0.0021 **). (*C4*) Peak duration increases when d_{shaft} decreases in nodes 1 (p-value=0.0051 **) and 2 (p-value=0.014 *). (*C5*) The frequency of $\mathrm{IP}_3\mathrm{R}$ opening increases when d_{shaft} decreases in both nodes 1 and 2 (***). Note that there were no Ca^{2+} peak in simulations with d_{shaft}=d_0. Ca^{2+} peak characteristics were not statistically different between node 1 and 2. Data are represented as mean ± STD, n=20 for each geometry. The effect of d_{shaft} on each Ca^{2+} signal characteristic was tested using one-way ANOVA. Significance is assigned by * for $p \leq 0.05$, ** for $p \leq 0.01$, *** for $p \leq 0.001$.

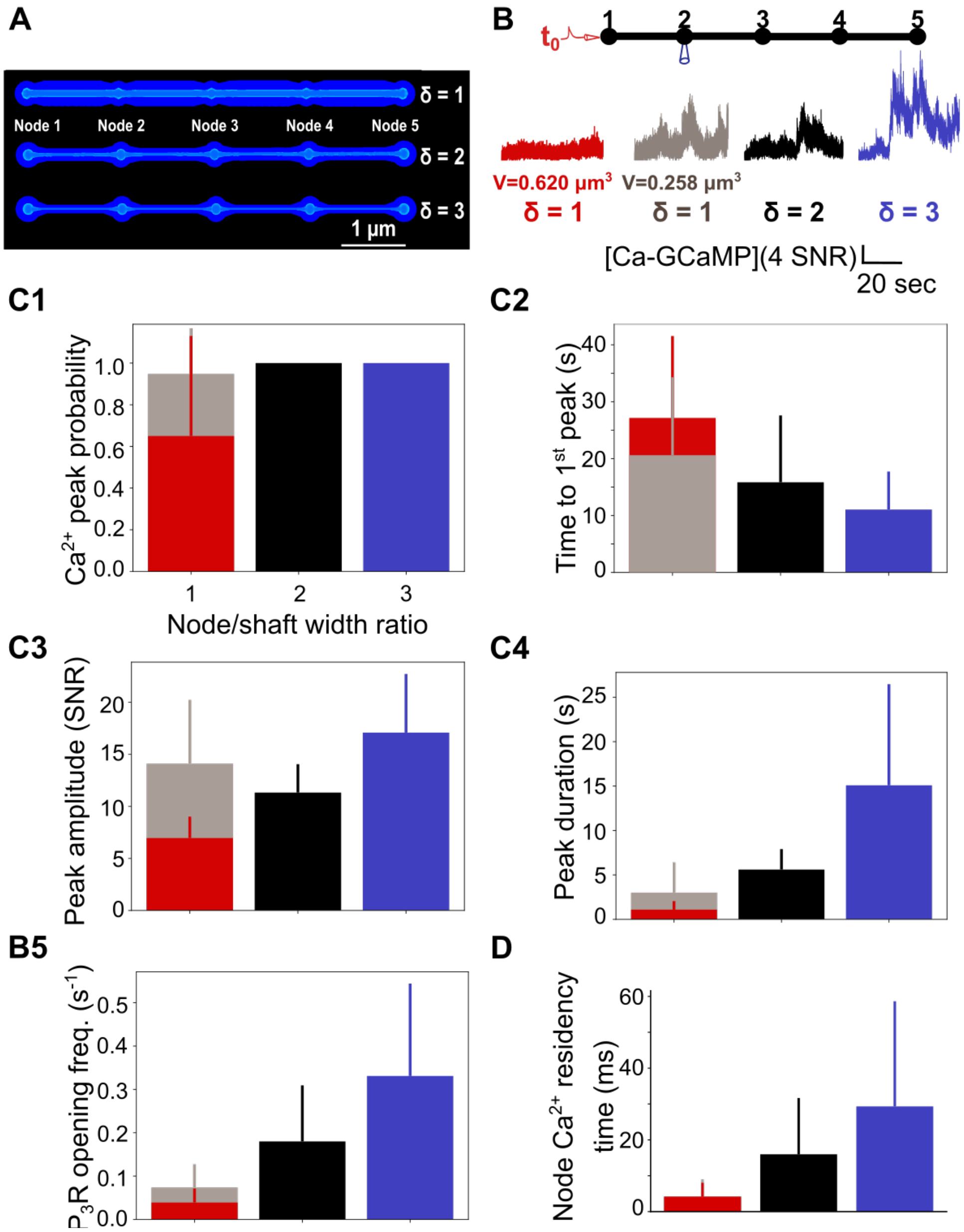

Figure 3–Figure supplement 4. Node/shaft width ratio and node volume control local Ca^{2+} activity. (*A*) Screenshots from STEPS visualization toolkit revealing meshes used in this study, that contain 5 identical nodes and 4 identical shafts. (*B*) (*Top*) Neuronal stimulation protocol simulated for each geometry: node 1 was stimulated at t=t_0=1s (k_{Ca}=0 s^{-1}), while Ca^{2+} activity was recorded in node 2. (*Bottom*) Representative Ca^{2+} traces in node 2 in geometries with node/shaft width ratio $\delta = \frac{d_0}{d_{shaft}}$ = 1 (red and gray), 2 (black) and 3 (blue), expressed as SNR (see Methods). Red and grey traces correspond to Ca^{2+} signals in geometries with δ=1 and a volume V_1=0.620 μm^3 and V_1=0.258 μm^3, respectively. Black and blue traces were recorded in geometries with V_2=0.263 μm^3 and V_3=0.195 μm^3, respectively. (*C*) Quantification of Ca^{2+} signal characteristics depending on node/shaft width ratio δ and on process volume. Data are represented as mean ± STD, n=20 for each geometry. (*C1*) Ca^{2+} peak probability does not vary with δ when V_1=0.258 μm^3 (p-value=0.22). (*C2*) Time to 1^{st} peak decreases with δ (p-value=0.0018 *). (*C3*) Peak amplitude does not vary with δ when V_1=0.258 μm^3 (p-value=0.16). (*C4*) Peak duration increases with δ, for both V_1=0.620 μm^3 and V_1=0.258 μm^3 (***). (*C5*) The frequency of IP_3R opening increases with δ, for both V_1=0.620 μm^3 and V_1=0.258 μm^3 (***). (*D*) Ca^{2+} residency time in nodes increases with δ, for both V_1=0.620 μm^3 and V_1=0.258 μm^3 (***, n=300). The effect of node/shaft width ratio on each Ca^{2+} signal characteristic was tested using one-way ANOVA. Significance is assigned by * for $p \leq 0.05$, ** for $p \leq 0.01$, *** for $p \leq 0.001$.

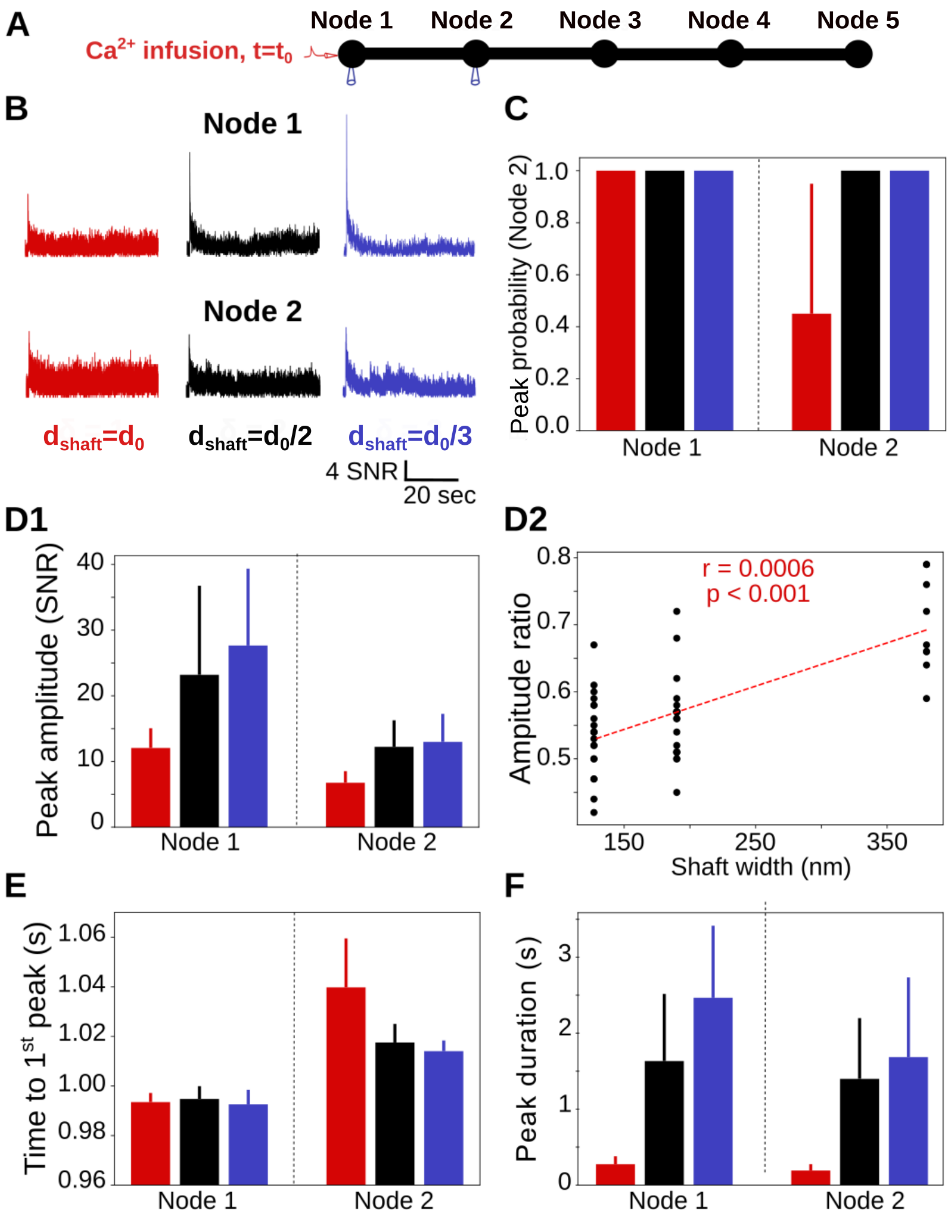

Figure 3–Figure supplement 5. Thin shafts enhance local spontaneous Ca^{2+} activity. (*A*) Neuronal stimulation protocol simulated for each geometry. 200 Ca^{2+} ions were infused in Node 1 at time t=t_0, while Ca^{2+} activity was recorded in nodes 1 and 2. (*B*) Representative Ca^{2+} traces in node 1 (top) and node 2 (bottom) for d_{shaft}=d_0 (red), $\frac{d_0}{2}$ (black) and $\frac{d_0}{3}$ (blue), expressed as SNR (see Methods). (*C*) Ca^{2+} peak probability increases when d_{shaft} decreases in node 2 (***). Note that peak probability is 1 in node 1 as the injection of 200 Ca^{2+} ions in node 1 results in a local Ca-GCaMP peak for all seed values tested. (*D1*) Peak amplitude increases when d_{shaft} decreases in node 1 (***) and 2 (***). (*D2*) The ratio between peak amplitude in node 2 and in Node 1 increases with shaft width (Spearman r=0.0006, p-value < 0.001 ***). (*E*) Time to 1^{st} peak in node 2 increases with d_{shaft} (***). Note that time to 1^{st} peak does not vary with d_{shaft} in node 1 as it occurs quickly after Ca^{2+} injection, through the binding of the injected Ca^{2+} ions to GCaMP molecules. (*F*) Peak duration increases when d_{shaft} decreases in node 1 (***) and 2 (***). Note that Ca^{2+} peak characteristics were not statistically different between nodes 1 and 2. Data are represented as mean ± STD, n=20 for each geometry. The effect of d_{shaft} on each Ca^{2+} signal characteristic was tested using one-way ANOVA. Significance is assigned by * for $p \leq 0.05$, ** for $p \leq 0.01$, *** for $p \leq 0.001$.

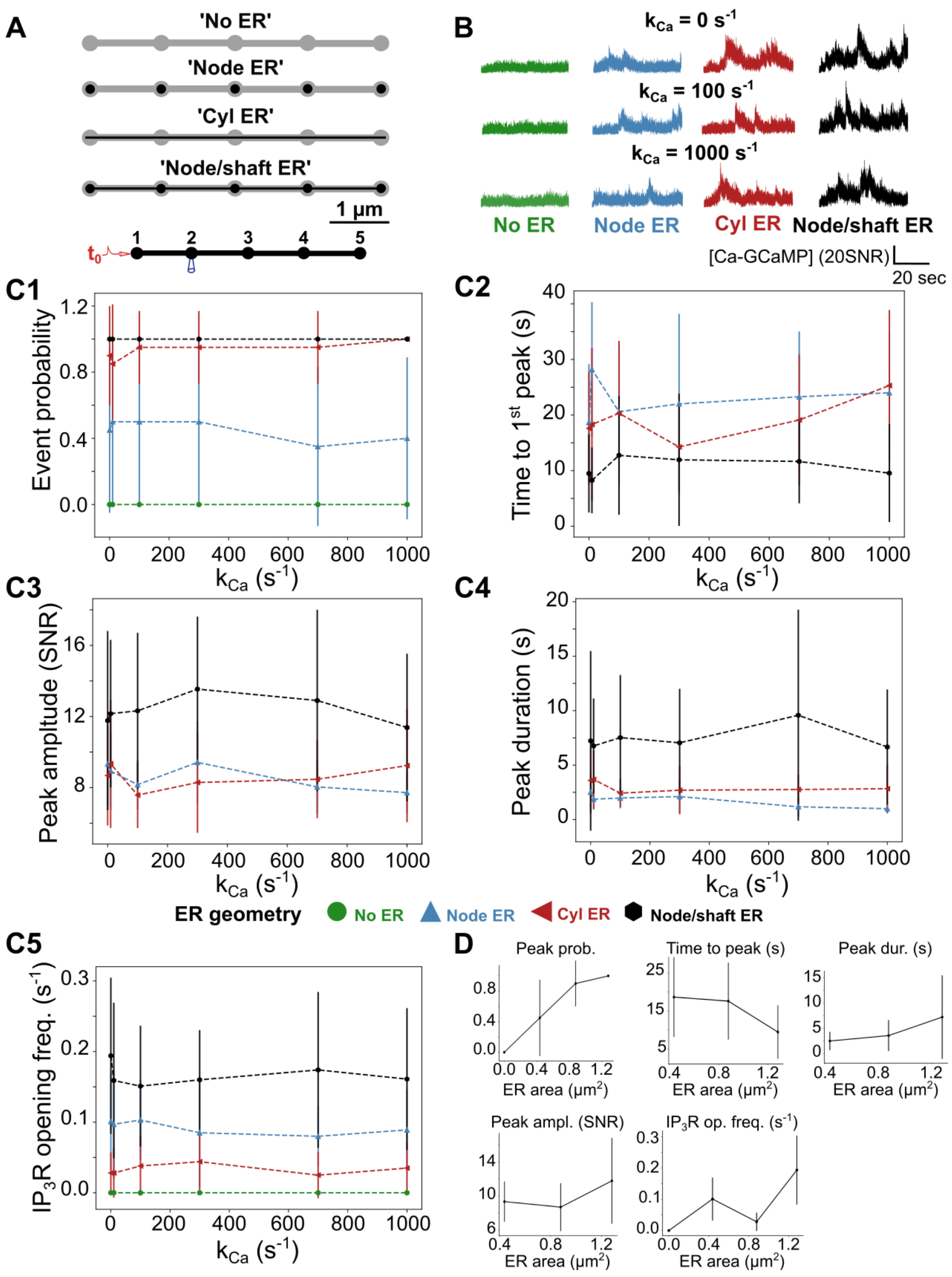

Figure 3–Figure supplement 6. **Ca^{2+} peak probability, amplitude and duration decrease with ER surface area.** (*A*) As the shape and distribution of the ER in fine processes have not been characterized in live tissue so far but are likely highly variable (***Aboufares El Alaoui et al., 2021***), simulations were performed in meshes with various ER shapes: “No ER”, “Node ER” and “Node/shaft ER”, in which there was no ER, discontinuous ER in nodes or an ER consisting in node/shaft alternations, respectively. (*B*) (*Top*) Neuronal stimulation protocol simulated for each geometry: node 1 was stimulated at t=t_0=1s, while Ca^{2+} activity was monitored in nodes 1 and 2. (*Bottom*) Representative Ca^{2+} traces in node 2, in “No ER” (green), “Node ER” (blue) and “Node/shaft ER” (black) geometries $d_{\text{shaft}} = \frac{d_0}{2}$, for k_{Ca}=0, 10, 100, 300, 700 and 1000 s^{-1}, expressed as SNR (see Methods). (*C*) Quantification of peak characteristics depending on ER geometry and k_{Ca}. Ca^{2+} peak probability (***, *C1*), time to 1^{st} peak (***, *C2*), peak amplitude (***, *C3*), duration (***, *C4*) and the frequency of IP$_3$R opening (***, *C5*) vary with the ER morphology. Note that Ca^{2+} peak characteristics did not vary with k_{Ca}. (*D*) Time to 1^{st} decreases as ER surface area increases (***) while Ca^{2+} peak probability (***), amplitude (***) and duration (***) as well as the frequency of IP$_3$R opening (***) increase as ER surface area increases, k_{Ca}=0 s^{-1}. Data are represented as mean ± STD, n=20 for each geometry. Significance is assigned by * for $p \leq 0.05$, ** for $p \leq 0.01$, *** for $p \leq 0.001$.

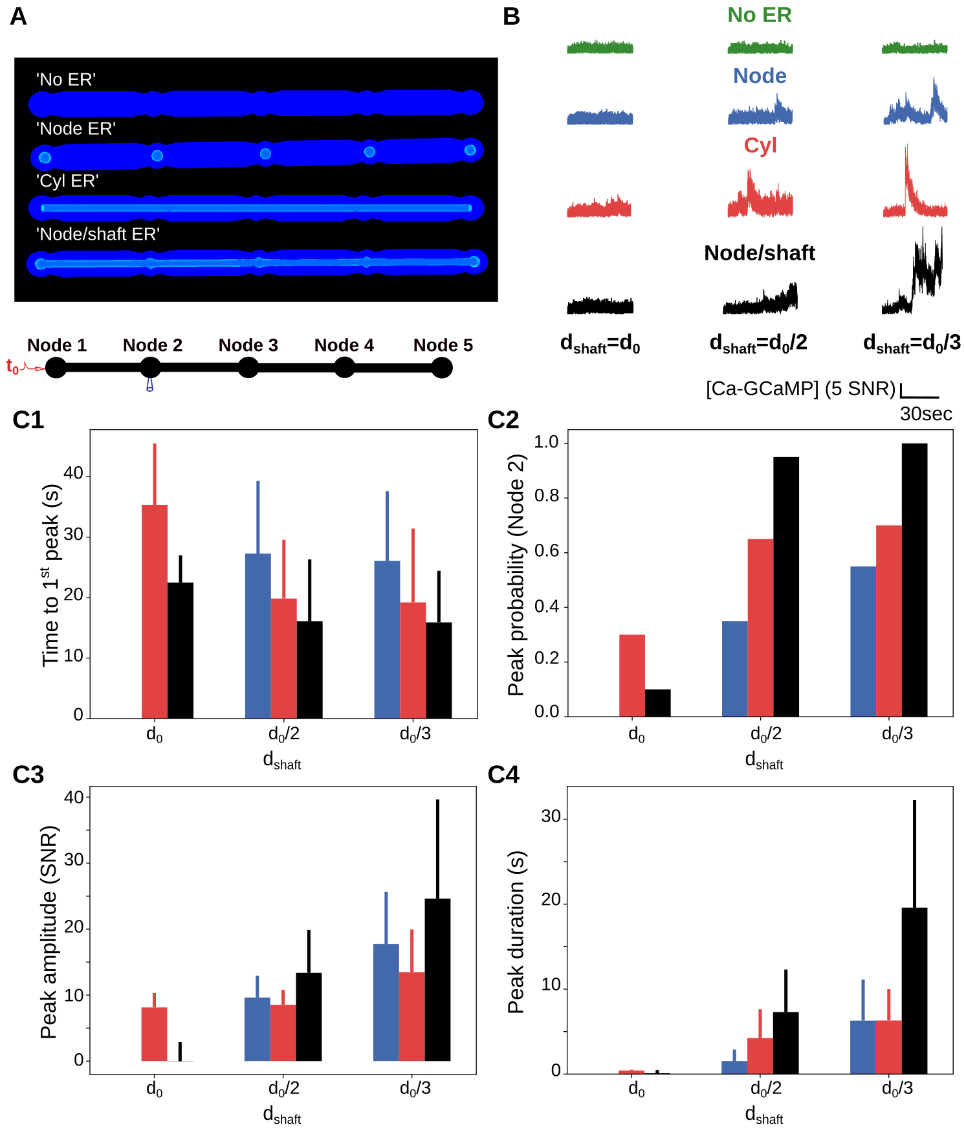

Figure 3–Figure supplement 7. Local Ca^{2+} activity increases when shaft diameter decreases, for all ER geometries tested. (*A*) Screenshots displaying the geometries used to investigate the effect of ER geometry on Ca^{2+} dynamics: "No ER", "Node ER", "Node/shaft ER" and "Cyl ER". (*B*) (*Top*) Neuronal stimulation protocol simulated for each geometry: node 1 was stimulated at t=t_0=1s (k_{Ca}=0 s^{-1}), while Ca^{2+} activity was monitored in node 2. (*Bottom*) Representative Ca^{2+} traces in node 2 for d_{shaft}=d_0 (left), $\frac{d_0}{2}$ (center) and $\frac{d_0}{3}$ (right), in "No ER" (green), "Node ER" (blue), "Cyl ER" (red) and "Node/shaft ER" (black) geometries, expressed as SNR (see Methods). (*C*) Quantification of the effect of d_{shaft} on Ca^{2+} dynamics. Note that no bar is visible for simulations in "Node ER" d_{shaft}=d_0 geometries as no peak was detected. Results in "Node/shaft ER" geometries are presented in Fig3 but are added here (black bars) for comparison. (*C1*) Time to 1^{st} peak in node 2 does not vary with d_{shaft} in "Node ER" simulations (p-value=0.85) but increases with d_{shaft} in "Cyl ER" simulations (p-value= 0.021 *). (*C2*) Ca^{2+} peak probability in node 2 increases when d_{shaft} decreases in "Node ER" simulations (***) and in "Cyl ER" simulations (p-value=0.01 *). (*C3*) Peak amplitude increases when d_{shaft} decreases in "Node ER" geometries (p-value=0.027 *) and in "Cyl ER" (p-value=0.01 *). (*C4*) Peak duration increases when d_{shaft} decreases in "Node ER" simulations (p-value=0.028 *) and in "Cyl ER" simulations (p-value=0.001 **). Data are represented as mean ± STD, n=20, for each geometry. The effect of d_{shaft} on each Ca^{2+} signal characteristic was tested using one-way ANOVA. Significance is assigned by * for $p \leq 0.05$, ** for $p \leq 0.01$, *** for $p \leq 0.001$.

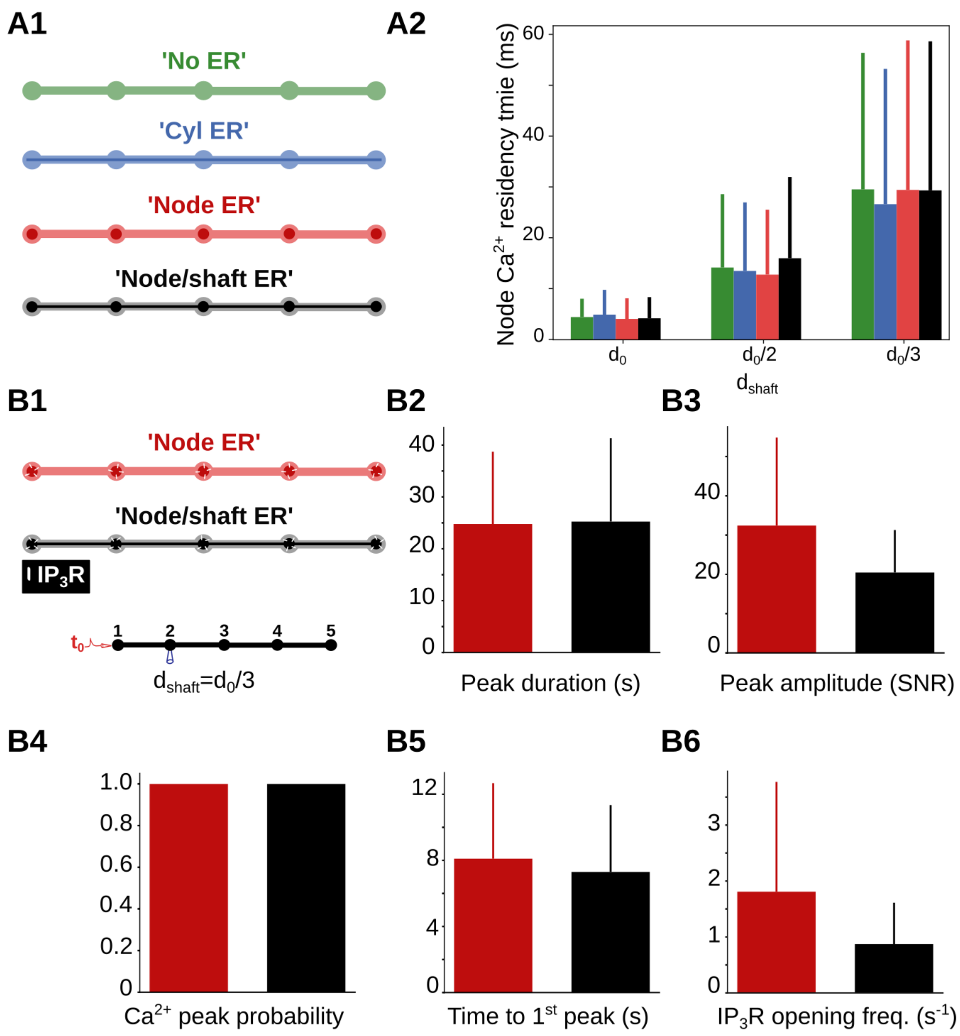

Figure 3–Figure supplement 8. Sensitivity study of the effect of ER morphology on Ca^{2+} dynamics. (A) Node Ca^{2+} residency time is not influenced by ER morphology. (A1) One Ca^{2+} ion was added in node 1 in geometries with different ER shapes: "No ER" (green), "Node ER" (blue), "Cyl ER" (red) and "Node/shaft ER" (black). (A2) For all ER shapes tested, Ca^{2+} residency time in nodes increases when d_{shaft} decreases. Node Ca^{2+} residency time does not change depending on ER morphology, suggesting that cellular morphology has a greater influence on compartmentalization than ER morphology in the meshes used in this study. Data are represented as mean $\leq$ STD, n=300 for each geometry. (B) Sensitivity study of the effect of ER morphology on Ca^{2+} dynamics with constant number of $\mathrm{IP_3}$Rs. (B1) Simulations were performed in 'Node ER' (red) and "Node/shaft ER" (black) geometries with $\mathrm{IP_3}$R channels (white) located in nodes (Top), resulting in a constant number of IP3R channels for both ER shapes. Node 1 was stimulated at t=t0=1s (k_{Ca}=0 s^{-1}), while Ca^{2+} activity was monitored in node 2 (bottom). (B2-6) Quantification of Ca^{2+} signals depending on ER morphology with constant number of $\mathrm{IP_3}$R in node 2, $d_{\mathrm{shaft}}=\frac{d_0}{3}$. Data are represented as mean $\leq$ STD, n=20 for each geometry. Ca^{2+} peak duration (B2), amplitude (B3), probability (B4) and delay (B5) do not vary with ER morphology when $\mathrm{IP_3}$R channels are located in nodes. (B6) $\mathrm{IP_3}$R opening frequency does not significantly differ between "Node ER" and "Node/shaft ER" geometries (p-value=0.06). Those results suggest that the decreased Ca^{2+} activity in branchlets that contain discontinuous ER reported in Fig 4 mainly results from the decreased number of $\mathrm{IP_3}$R channels associated with the decreased ER surface area of "Node ER" compared to "Node/shaft ER" morphology.

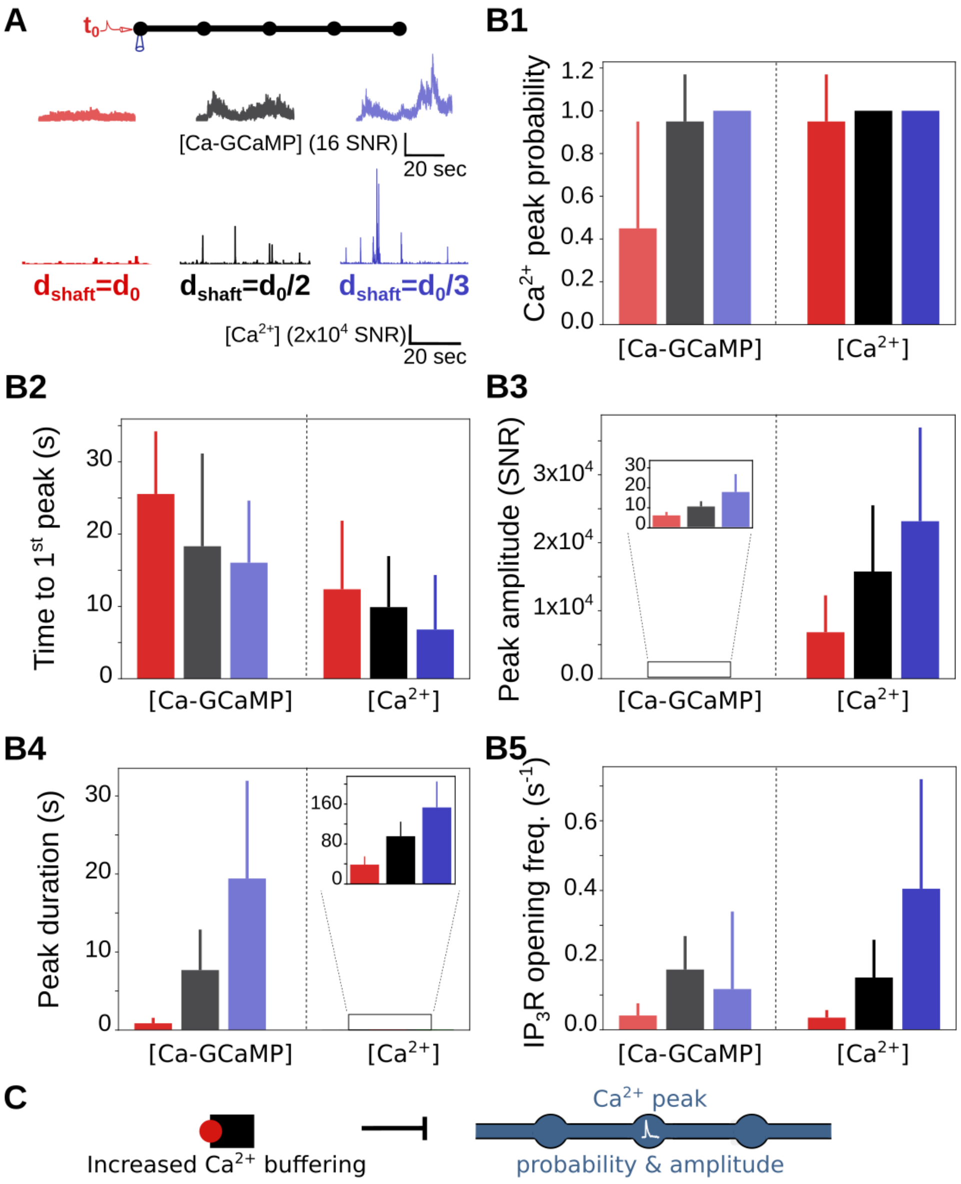

Figure 3–Figure supplement 9. Ca^{2+} **indicators alter** Ca^{2+} **peak characteristics.** (*A*) In order to investigate free Ca^{2+} peak probability, no GCaMP molecules were added to the model. (*Top*) At t=t_0=1s, node 1 was stimulated (k_{Ca}=0 s^{-1}), while Ca^{2+} concentration was monitored in node 1. The geometry used for $d_{\text{shaft}}=d_0$ corresponds to the geometry presented in Fig 1A. (*Middle*) Representative Ca-GCaMP traces in node 1, in simulations containing GCaMP molecules in geometries with shaft width $d_{\text{shaft}} = d_0$ (light red), $\frac{d_0}{2}$ (grey) and $\frac{d_0}{3}$ (light blue). (*Bottom*) Representative free Ca^{2+} traces in node 1, in the absence of GCaMP molecules, in geometries with shaft width $d_{\text{shaft}} = d_0$ (red), $\frac{d_0}{2}$ (black) and $\frac{d_0}{3}$ (blue). The amplitude of Ca-GCaMP and free Ca^{2+} signals is expressed as SNR (see Methods). (*B*) Characteristics of free Ca^{2+} signals depending on d_{shaft}. Ca-GCaMP signals measured in simulations from Fig 3 are presented for comparison. (*B1*) Free Ca^{2+} peak probability does not vary with d_{shaft} (p-value=0.22). Ca-GCaMP peak probability is lower than free Ca^{2+} peak probability for $d_{\text{shaft}}=d_0$ (***). (*B2*) Time to 1^{st} free Ca^{2+} peak increases with d_{shaft} (***). Time to 1^{st} Ca-GCaMP peak is higher than time to 1^{st} free Ca^{2+} peak, for any value of d_{shaft} (***). (*B3*) Free Ca^{2+} peak amplitude increases when d_{shaft} decreases (***). Ca-GCaMP peak amplitude is lower than free Ca^{2+} peak amplitude, for any value of d_{shaft} (***). (*B4*) Free Ca^{2+} peak duration increases when d_{shaft} decreases (***). Ca-GCaMP peak duration is higher than free Ca^{2+} peak duration, for any value of d_{shaft} (***). (*B5*) The frequency of IP$_3$R opening increases when d_{shaft} decreases (***). (*C*) Schematic summarizing the main result from this figure: increased Ca^{2+} buffering is associated with decreased Ca^{2+} peak probability and amplitude. Data are represented as mean ± STD, n=20 for each geometry. The effect of d_{shaft} on each free Ca^{2+} signal characteristic was tested using one-way ANOVA. Significance is assigned by * for $p \leq 0.05$, ** for $p \leq 0.01$, *** for $p \leq 0.001$.

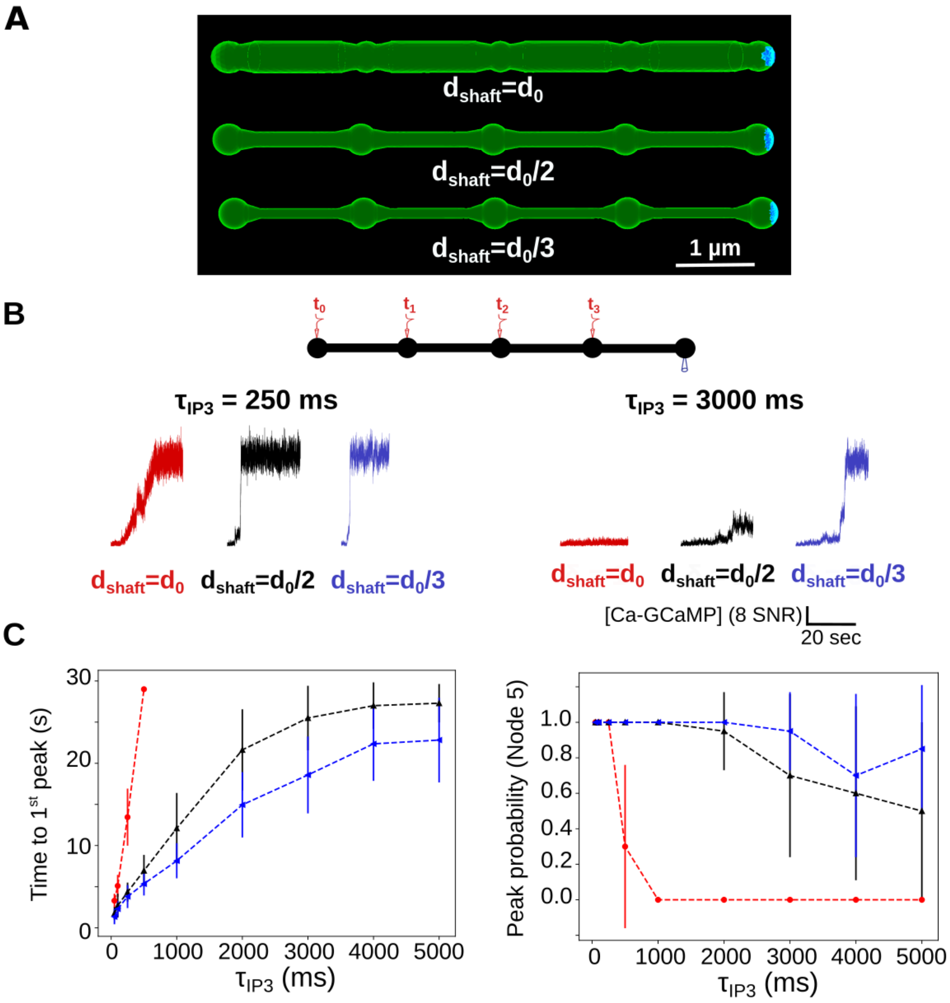

Figure 5–Figure supplement 1. Sensitivity study of the effect of boundary conditions on local Ca^{2+} activity upon repeated neuronal stimuli. (*A*) Simulations were performed in the “5nodes” geometries (Fig1). Boundary conditions were absorbing at the extremity of node 5 (blue) while the remaining boundaries were characterized by reflective boundary conditions (green). Those boundary conditions mimic the connection of the modeled astrocyte branchlet to the rest of the cell. (*B*) (*Top*) node 1 was stimulated at t=t_0=5s, node 2 at $t_0+\tau_{\mathrm{IP3}}$, node 3 at $t_0+2\tau_{\mathrm{IP3}}$ and node 4 at $t_0+3\tau_{\mathrm{IP3}}$, k_{Ca}=0 s^{-1}, while Ca^{2+} activity was monitored in node 5. (*Bottom*) Representative Ca^{2+} traces for d_{shaft}=d_0 (red), $\frac{d_0}{2}$ (black) and $\frac{d_0}{3}$ (blue), with τ_{IP3}=250ms (left) and 3000ms (right), expressed as SNR (see Methods). (*C*) (*Left*) Time to 1^{st} peak in node 5 increases with τ_{IP3} for d_{shaft}=d_0 (***), d_{shaft}=$\frac{d_0}{2}$ (***) and d_{shaft}=$\frac{d_0}{3}$ (***). Time to 1^{st} peak is higher for d_{shaft}=d_0 compared to d_{shaft}=$\frac{d_0}{2}$ and d_{shaft}=$\frac{d_0}{3}$. (*Right*) Ca^{2+} peak probability in node 5 is lower for d_{shaft}=d_0 compared to d_{shaft}=$\frac{d_0}{2}$ and d_{shaft}=$\frac{d_0}{3}$ and decreases as τ_{IP3} increases for d_{shaft}=d_0 (***) and d_{shaft}=$\frac{d_0}{2}$ (***) but not d_{shaft}=$\frac{d_0}{3}$ (p-value=0.054). Note that Ca^{2+} peak probability was lower and time to 1^{st} peak higher compared to simulations with reflective boundary conditions. Data are represented as mean ± STD, n=20 for each value of d_{shaft} and of τ_{IP3}. Lines are guides for the eyes. The effect of d_{shaft} on each Ca^{2+} signal characteristic was tested using one-way ANOVA. Significance is assigned by * for $p \leq 0.05$, ** for $p \leq 0.01$, *** for $p \leq 0.001$.